

The novel properties of SF₆ for directional dark matter experiments

N. S. Phan*, R. Lafler, R. J. Lauer, E. R. Lee, D. Loomba, J. A. J. Matthews and E. H. Miller

Department of Physics and Astronomy, University of New Mexico, NM 87131, USA

Abstract

SF₆ is an inert and electronegative gas that has a long history of use in high voltage insulation and numerous other industrial applications. Although SF₆ is used as a trace component to introduce stability in tracking chambers, its highly electronegative properties have limited its use in tracking detectors. In this work we present a series of measurements with SF₆ as the primary gas in a low pressure Time Projection Chamber (TPC), with a thick GEM used as the avalanche and readout device. The first results of an ⁵⁵Fe energy spectrum in SF₆ are presented. Measurements of the mobility and longitudinal diffusion confirm the negative ion drift of SF₆. However, the observed waveforms have a peculiar but interesting structure that indicates multiple drift species and a dependence on the reduced field (E/p), as well as the level of water vapor contamination. The discovery of a distinct secondary peak in the waveform, together with its identification and use for fiducializing events in the TPC, are also presented. Our measurements demonstrate that SF₆ is an ideal gas for directional dark matter detection. In particular, the high fluorine content is desirable for spin-dependent sensitivity, negative ion drift ensures low diffusion over large drift distances, and the multiple species of charge carriers allow for full detector fiducialization.

1 Introduction

Sulfur hexafluoride (SF₆) is an inert, odorless, and colorless gas commonly known as an electron scavenger because of its large electron attachment cross-section [1, 2, 3, 4, 5, 6, 7, 8, 9]. The high electron affinity coupled with its non-toxicity and non-flammability make it suitable for use in many practical applications, including as a gaseous dielectric insulator in high voltage power devices, plasma etching of silicon and Ga-As based semiconductors, thermal and sound insulation, magnesium casting, and aluminum recycling (Refs. [10, 11] provide an extensive review of the properties and applications of SF₆). In particle detectors, SF₆ has been used as a quencher in Resistive Plate Chambers (RPCs) operated in both avalanche and streamer modes, enabling more stable operation by suppressing streamer formation in the former, and reducing the energy of discharges and allowing lower voltage operation in the latter [12, 13]. As a result of its many diverse commercial and research applications, SF₆ is one of the most extensively studied gases [10].

*nphan@unm.edu

Nevertheless, with the exception of RPCs, studies of SF₆ in conditions applicable to particle physics detectors are scarce. Although SF₆ was considered as a negative ion gas in rare searches [14], the high electron affinity was deemed a barrier for stripping the electron from the negative ion in the avalanche region, a necessary first step for initiating gas gain amplification. However, with the advent of Micro-patterned Gas Detectors (MPGDs), which have flexible geometries that can sustain high electric fields in the avalanche region even at low pressures, the potential for achieving gas gain in SF₆ may be realized. Demonstrating this for low energy event detection would open up the possibility for its use in a variety of experiments, such as directional dark matter searches. Our work provides the first experimental evidence that SF₆ is in fact an excellent choice as a negative ion gas for TPC-based directional dark matter experiments.

Directional searches in TPCs require low pressures, to lengthen recoil tracks, and low diffusion so they can be resolved, both of which are ideally suited to negative ion gases. The idea of negative ion drift with carbon disulfide (CS₂) was first proposed by Martoff to circumvent the use of magnetic fields to achieve low diffusion in large TPCs [15]. Negative ion TPCs were first successfully demonstrated with CS₂-based gas mixtures by DRIFT, a directional dark matter experiment [16, 17]. At present DRIFT employs a mixture of 30:10:1 Torr CS₂:CF₄:O₂, which leverages the benefits of negative-ion CS₂ with the spin content of fluorine, an ideal target for spin-dependent (SD) interactions with WIMPs¹, and the capability to fiducialize the detector provided by O₂ [19]. This multi-component DRIFT gas mixture was tailored for directional DM searches where low diffusion, low backgrounds and the SD limit-setting capabilities are all essential.

As demonstrated in this work, SF₆ has all of benefits of the DRIFT gas mixture, along with additional advantages that make it more amenable to the underground environment. We begin by discussing the motivation behind, and benefits of each component of the CS₂/CF₄/O₂ gas mix for directional dark matter experiments, and how these are matched by SF₆.

In a detector with an electronegative gas, like CS₂, the free electrons produced by an ionization event are quickly captured, forming anions that drift in the thermal regime to the amplification and readout region. In this regime, diffusion scales as $\sqrt{L/E}$, where L is the drift distance and E is the strength of the drift field, making it desirable to have high fields to minimize diffusion. With this, good tracking resolution can be achieved over long drift distances, which are two necessary conditions for the high quality track reconstruction and large detection volumes required for directional dark matter and other rare event searches. Like CS₂, which has an electron affinity of 0.55 eV [20], SF₆ is highly electronegative with electron affinity of 1.06 eV [21].² Thus, SF₆ should also behave like a negative ion gas, with similar drift properties to CS₂.

An additional advantage of electronegative gases is that they tend to display superior high voltage performance at low pressures over electron drift gases, such as CF₄ and N₂. SF₆ is especially well suited in this regard, having a breakdown field strength that is about three times higher than air [25] and N₂ [26, 27] at pressures below one atmosphere.

The CF₄ in the DRIFT gas mixture, as mentioned above, provides the fluorine target for SD WIMP interactions. In this regard, with its high fluorine content, SF₆ has a clear advantage over CS₂/CF₄ mixtures for SD searches. Thus, if the potential of SF₆ as a negative ion gas are borne out, there would be no need to sacrifice precious detection volume to the non spin-dependent CS₂, leading to a significant increase in the sensitivity to dark matter.

The motivation for O₂ in the DRIFT gas mixture came from the recent discovery that the combination CS₂/O₂ produces features in the signal waveform that allow event fiducialization

¹For SD dark matter searches neither ¹²C or ³²S atoms have the nuclear spin content to be suitable detection targets, whereas ¹⁹F is excellent in this regard [18]

²The values quoted for SF₆ were recommended by Ref. [21] based on results from Ref. [22] and Ref. [23], and the value for CS₂ is the most precise to date. Note however that, similar to SF₆, the experimentally determined electron affinities of CS₂ have a large spread, ranging from $\sim 0.5 - 1.0$ eV [24].

[19]. This enabled the ability to reject backgrounds from detector surfaces, a critical advance for gas TPCs used in rare searches. With this, DRIFT demonstrated a ~ 50 day, zero background limit that is currently the world's best for a directional experiment [17]. We show in Section 3 that the signal waveform in SF_6 also contains similar features that can be used for fiducialization (Section 7).

There are a number of other advantages of SF_6 over $\text{CS}_2/\text{CF}_4\text{O}_2$ mixtures. One is the ability to purify via recirculation, which has not been demonstrated to satisfaction with any CS_2 mixture but should be straightforward with SF_6 . This would lower backgrounds and also lower costs and the manpower needed for transporting gas underground. With respect to safe underground operations another advantage of SF_6 is its non-toxicity and non-flammability, whereas CS_2 is highly toxic and, with the addition of O_2 , flammable and potentially explosive [28]. CS_2 also has a tendency to be absorbed into detector surfaces making operation and maintenance arduous. Finally, SF_6 has an extremely high vapor pressure of 15,751 Torr at room temperature, compared to about 300 Torr for CS_2 .

In order to realize the very appealing prospects of SF_6 , the key features we need to demonstrate in this work are:

1. Gas amplification and the efficient stripping of the electron from SF_6^- in the gain stage.
2. Gas gain and its dependence on pressure. For example, if good gas gain can be achieved at high pressure, it would have implications for double-beta decay searches with SeF_6 (selenium hexafluoride), which has a similar molecular structure [29].
3. Low thermal diffusion in SF_6 , as expected from a negative ion gas, and how it compares to CS_2 .
4. Features in the signal waveforms that could be used to fiducialize events along the TPC's drift direction.

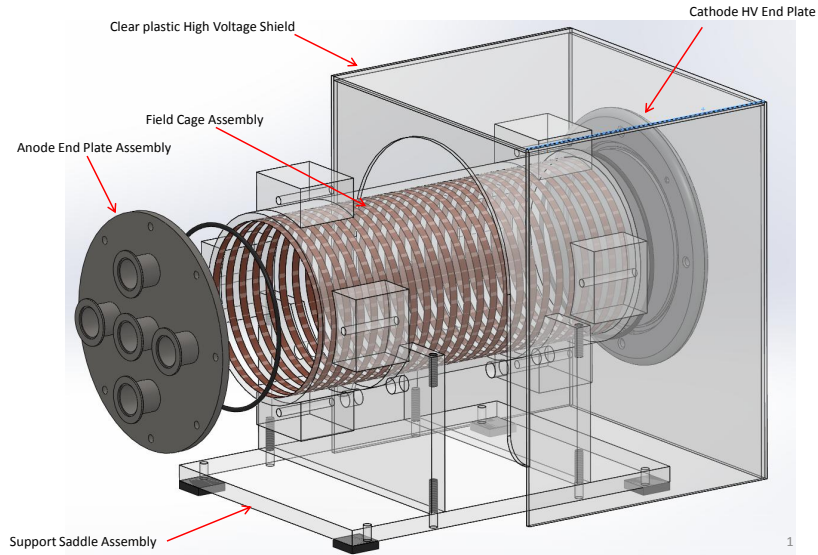
2 Experimental apparatus and method

2.1 Acrylic detector

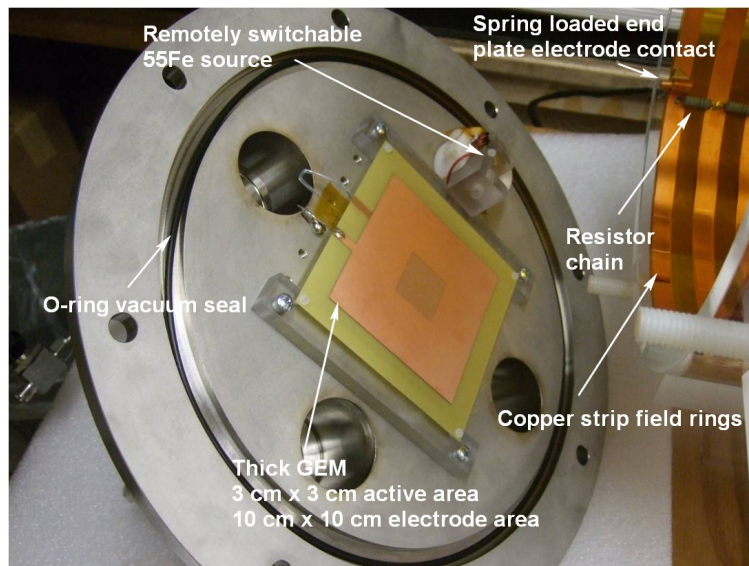
The TPC detector used to make measurements for this work (Figure 1) consisted of a 60 cm long acrylic cylinder with an inner diameter of 30.5 cm. The two ends of the detector were made from aluminum plates, one serving as the cathode that could be powered up to a maximum voltage of -60 kV, and the other as the grounded anode. The acrylic TPC with its aluminum end-caps also served as the vacuum vessel. The field rings were made from a kapton PC flex board with 1.3 cm wide copper strips placed at a pitch of 2.54 cm and connected to 23 (56 M Ω) resistors. Gas amplification was provided by a single 0.4 mm thick GEM (THGEM) that was custom fabricated at CERN with an active area of 3×3 cm². The THGEM had a hole pitch of ~ 0.5 mm and hole diameter of ~ 0.3 mm, with an annular region of thickness 0.05 mm etched around the holes to eliminate burring from the drilling process. The THGEM was mounted on two acrylic bars attached to the anode plate. The surface of the THGEM facing the cathode was grounded to the anode plate while the other surface was held at high voltage (610 – 1020 V). Signals were read out from the high voltage surface with an ORTEC 142 charge sensitive preamplifier, which had a 20 ns rise-time (at zero capacitance) and a 100 μ s decay time constant.

2.2 Charge generation

Ionization was introduced into the gas volume either with an internally mounted and remotely switchable ^{55}Fe 5.89 keV X-ray source (Figure 1b), or by a system using a Stanford Research Systems (SRS) NL100 337.1 nm pulsed nitrogen laser, which was used to produce photoelectrons



(a) Acrylic cylindrical detector



(b) Inner view of anode end plate

Figure 1: (a) A schematic of the detector showing its primary cylindrical acrylic body, field cage, aluminum end plates, support saddle, and high voltage shield. The laser (not shown) sits near the anode plate and fires pulses through a quartz window onto the cathode to create photoelectrons at a known location. (b) A photograph of the inner side of the anode plate which shows the O-ring, switchable ^{55}Fe source, and THGEM.

by illuminating the aluminum cathode. The NL100 laser had a FWHM pulse width of 3.5 ns, a pulse energy of 170 mJ, and a peak power of 45 kW. The spot size in the longitudinal, or drift, dimension was essentially a delta function, whereas the projected spot size in the X and Y (lateral) dimensions was a 1×3 mm² rectangle. Measurements of transverse diffusion require an instrumented XY readout, which is the subject of future work.

2.3 Operation and data acquisition

After the vacuum vessel was sealed, a long pump-down with an Edwards XDS10 dry scroll vacuum pump (base pressure < 0.1 Torr) was conducted to minimize out-gassing from the acrylic cylinder and other components inside the detector. The vessel was then back-filled with approximately 200 Torr of SF₆ gas (99.999% purity), and flushed. This was done to dilute any residual out-gassed contaminants that the vacuum pump was not able to remove. The vessel was once again back-filled with gas to approximately 200 Torr and slowly pumped down to the final operating pressure, with a precision of 0.05 Torr. During this slow pump down, both the cathode and GEM were ramped up to operating voltages. This procedure assured a minimum time between the introduction of fresh gas into the detector and the start of data acquisition.

As the various measurements of SF₆ properties were performed as a function of the operating pressure and drift field, these were changed between each setting. This was done by raising the pressure back up to 200 Torr and, as before, slowly pumping down to the new pressure setting while concurrently setting the new cathode voltage. This procedure was repeated between each set of measurements, and its importance will be explained in Section 3.3 where the presence and effects of water vapor are discussed.

Although the focus of this paper is on SF₆, for comparative purposes we also present measurements of CS₂ properties made using the same setup. For this gas, the operating procedure was different than the one used for the SF₆. After the long pump down, the detector was back-filled to the operating pressure and all sets of measurements were taken without a pressure raise and pump down between each setting. When the cathode was brought to full operating voltage, a spark-down period of 30 – 60 minutes allowed micro-sparks due to the acrylic charging-up to subside before powering up the THGEM to full voltage.

All measurement waveforms were acquired with a Tektronix TDS 3054C digital oscilloscope and National Instruments data acquisition software, where every triggered event was read out and saved to file for analysis. The saved files contain the voltage signals from the ORTEC charge sensitive preamplifier, which integrated the charge collected by the THGEM readout surface with a rise time of ~ 100 ns, and an exponential decay time constant of $\tau = 100$ μ s. The current, $I(t)$, entering the preamplifier is related to the detected voltage signal, $V(t)$, by

$$I(t) \propto \frac{dV}{dt} - \left(-\frac{V}{\tau} \right), \quad (1)$$

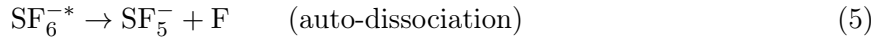
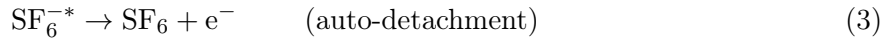
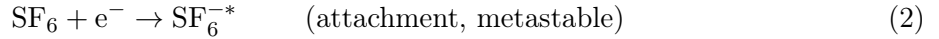
where the second term is for removing the decay tail. We used Equation 1 to compute $I(t)$ from our measurements of $V(t)$. After the conversion, pulses were smoothed with a Gaussian filter to suppress high frequency noise and to improve signal to noise. We then extracted the drift speed, diffusion, and other quantities from these processed waveforms.

3 SF₆ waveforms

3.1 Capture and transport in SF₆

Measurements made under differing conditions have shown that electron capture by the electronegative SF₆ molecule occurs rapidly [1, 2, 3, 4, 5, 6, 7, 8, 9] with the immediate product being

SF_6^{-*} , a metastable excited state of the anion, SF_6^- . The latter forms subsequently from the collisional or radiative stabilization of the excited state [11]. The electron capture cross-sections by SF_6 are very large [1, 2, 3, 4, 5, 6, 7, 8, 9] and estimates of the capture mean-free-path are about a micron at the pressures and drift fields of our experiments. This assumes that the electrons produced by the laser illumination of the cathode have near zero kinetic energies, where the capture cross-sections peak. The metastable SF_6^{-*} leads to subsequent products besides SF_6^- , whose relative abundances depend on the lifetime of SF_6^{-*} , the electron energy, gas pressure, temperature, and drift field:



Thus, after the quick electron capture leading to SF_6^{-*} , the auto-detachment reaction (3) will compete with collisional stabilization, reaction (4), and auto-dissociation, reaction (5). To determine whether auto-detachment plays a significant role in our experiment, which could lead to a significant distortion of the waveform, we consider bounds on the lifetimes of these reactions.

Measurements of lifetimes for auto-detachment have a broad range, from ~ 10 μs to one ms, depending on the experimental technique used. Under collision-free conditions, time-of-flight (TOF) mass spectrometric experiments indicate the lifetime is between 10 – 68 μs [30, 31, 32, 33, 34, 35]. Measurements made with ion cyclotron resonance (ICR) experiments, however, give lifetimes in the ms range [36, 37, 38]. The difference in measured lifetimes between the two techniques reflect different electron energies, with those in ICR experiments typically much lower than in TOF experiments [11], and closer to the energies in our experiment.

The lifetime for collisional stabilization (4) depends on the cross-section and collision rate. The former is large, and the latter can be estimated by considering the collision mean-free path, λ , for SF_6^{-*} in SF_6 . Assuming that this is similar to that of SF_6^- in SF_6 , we can use:

$$\lambda = \frac{(3MkT)^{1/2} v_d}{eE} \quad (6)$$

[39], where $T = 296$ K, M is the mass of the SF_6 molecule, v_d is the drift speed, and E is the drift field. Using our measured drift speeds (see Section 4) we estimate $\lambda \sim 0.1 - 1$ μm , implying a collisional mean-free time of $\sim 1 - 10$ ns. This is many orders of magnitude less than the lifetimes for auto-detachment, indicating that the latter process should be inconsequential in our experiment. This is confirmed by our waveforms shown in Section 3.2.

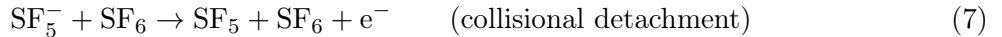
Besides reactions (4) and (5), which lead to the production of SF_6^- and SF_5^- , other processes occurring at either the site of initial ionization or during drift to the anode can lead to additional negative ion species. For example, the metastable SF_6^{-*} produced initially can also lead to F^- and SF_4^- (e.g., via auto-dissociation [11]), although at much lower probabilities; reactions producing these species have much lower production cross-sections and require much higher electron energies than those for SF_6^- and SF_5^- [40, 41, 42, 43]. Therefore, in our experiment we expect the initial charge carriers to be dominated by SF_5^- and SF_6^- , with their relative contributions estimated from production cross-sections.

The cross-section for reaction (4) is peaked at zero electron energy [43, 44, 45, 46], falling by a factor of about 100 at 0.1 eV [42, 43, 47], whereas that for reaction (5) has a peak at zero eV

[47] and a smaller one at ~ 0.38 eV [42, 43, 47]. At zero eV, the SF_6^- cross-section is larger by a factor 1000 than that for SF_5^- , but only a factor ~ 30 at 0.1 eV because the SF_6^- cross-section falls much more rapidly with energy than that of SF_5^- . For the low electron energies expected in our experiments, however, SF_6^- should be the dominant charge carrier arriving at the anode. Because of the higher mobility of SF_5^- ([48, 49, 50], and see Section 4 below) we should detect two peaks in the signal waveform, with the faster SF_5^- arriving earlier in time. This is the basis for fiducialization, and is discussed in detail in Section 7.

A number of possible reactions involving the drifting SF_5^- and SF_6^- with the neutral gas could, however, complicate this simple picture. At low drift fields, neutral, electron-hungry SF_6 molecules will form clusters around the negative ions [48]. Clusters of $\text{SF}_6^-(\text{SF}_6)_n$ and $\text{SF}_5^-(\text{SF}_6)_n$ ($n = 1, 2, 3, \dots$) have been observed but with mobilities less than those of SF_5^- and SF_6^- [48]. This phenomena could therefore partly explain the long tail observed on the slow side of the SF_6^- peak in our low reduced field waveforms (Figure 4a).

In addition to clustering, the drifting SF_5^- and SF_6^- could also interact with the neutral molecules or contaminants in the gas leading to other species (see Section 3.3). These could appear as distinct features in our measured waveforms. More important for us is the collisional detachment of energetically stable SF_5^- and SF_6^- via the following reactions:



Such processes would be followed by re-attachment via reaction (2), and the subsequent reactions (4) and (5) that lead back to SF_5^- or SF_6^- . The attachment/detachment of the electron could result in a smeared waveform due to the different drift speeds of the charge carriers. However, the probability of detachment via reactions 7 and 8 is very small for center-of-mass energies < 60 eV [51]. In comparison to the electron affinity of SF_5 (2.7 – 3.7 eV) [52] and SF_6 (1.06 eV), the threshold energy for detachment is much larger and is attributed to competing charge-transfer and collision-induced dissociation processes [51, 53, 54]. Nevertheless, there is evidence that energetically unstable states of SF_6^- (i.e. SF_6^{-*}) can contribute to collisional detachment [51, 53]. The relative contributions of these effects depend on the interaction energies at different reduced fields, but the detailed mechanisms is well beyond the scope of this work.

3.2 Waveform features

With an overview of the chemistry of electron drift and attachment in SF_6 , we now turn to a detailed look at our data. Shown in Figures 2 and 3 are the averaged current waveforms acquired in 20 Torr SF_6 ($N = 6.522 \times 10^{17} \text{ cm}^{-3}$ at $T = 296$ K) for six different drift field strengths. The averaging was done using one thousand individual waveforms, each acquired by illuminating the cathode with the nitrogen laser. The laser also provided the initial trigger for the DAQ system.

At low fields, the waveform consists of two peaks, one much smaller than the other, and a low amplitude broad component distributed outside the region of the two peaks. The large main peak is SF_6^- and the smaller secondary peak arriving earlier is SF_5^- . The non-peak component does not appear continuous but displays a step in amplitude at the location of the smaller peak, and a second step to the baseline at an earlier time. With increasing field strength, this non-peak component gradually subsides until it is barely discernible at $E = 1029 \text{ V}\cdot\text{cm}^{-1}$ (Figure 3f) leaving just the two sharp peaks. The origin of this component is water vapor contamination from out-gassing in the acrylic vessel, and is subject of Section 3.3.

The waveforms show a similar behavior as a function of inverse pressure, $1/p$. Figure 4 shows portions of waveforms taken at three pressures with a fixed drift field, $E = 86 \text{ V}\cdot\text{cm}^{-1}$, the lowest used in our experiment. The broad component decreases relative to the main SF_6^- peak as the

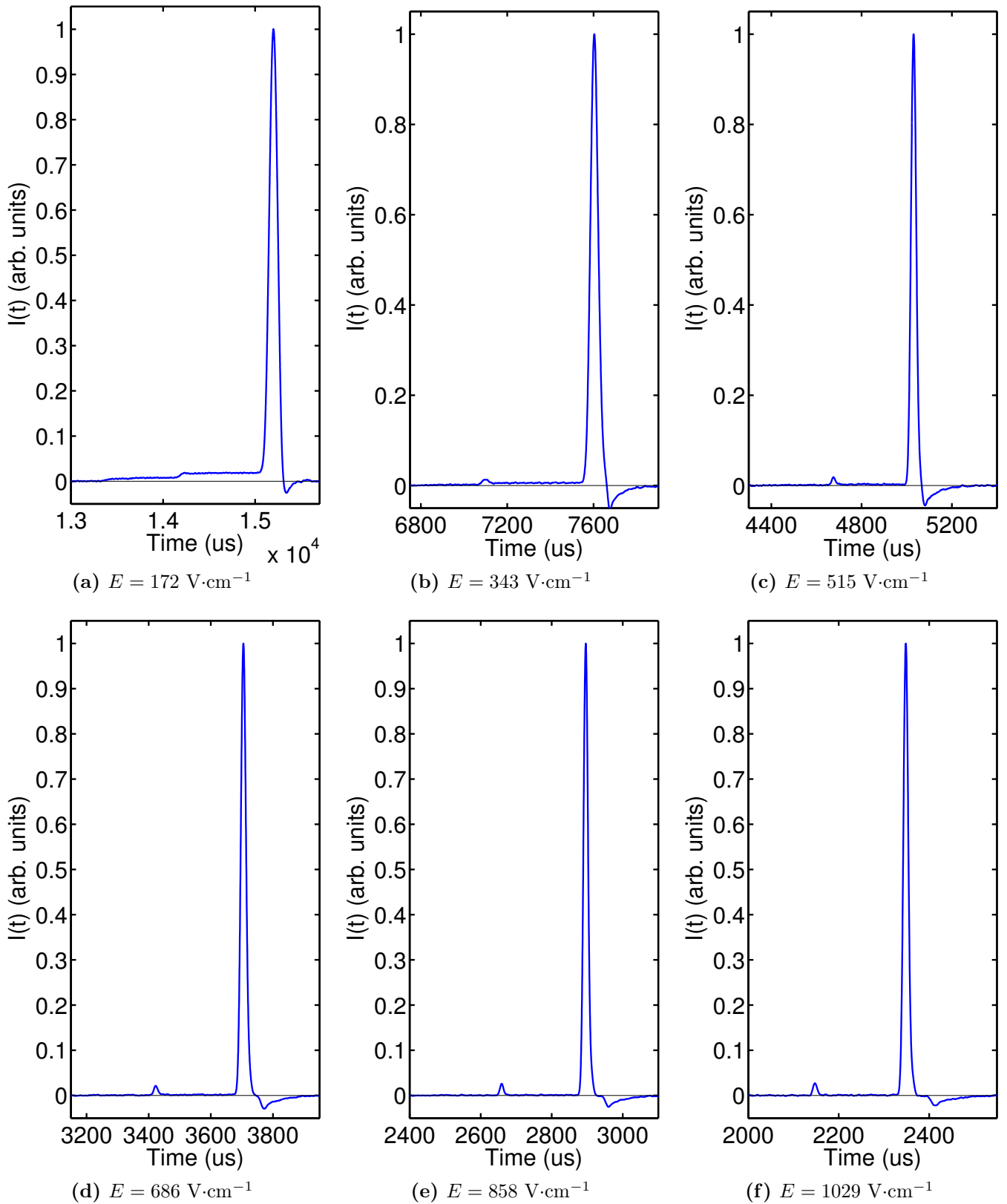


Figure 2: (a) - (f) The average waveforms acquired in 20 Torr SF₆ at six different electric fields. At low fields (a), there is an additional broad structure in addition to the two peaks. This component appears to decrease in magnitude with increasing electric field and seemingly vanishes at the highest field (f).

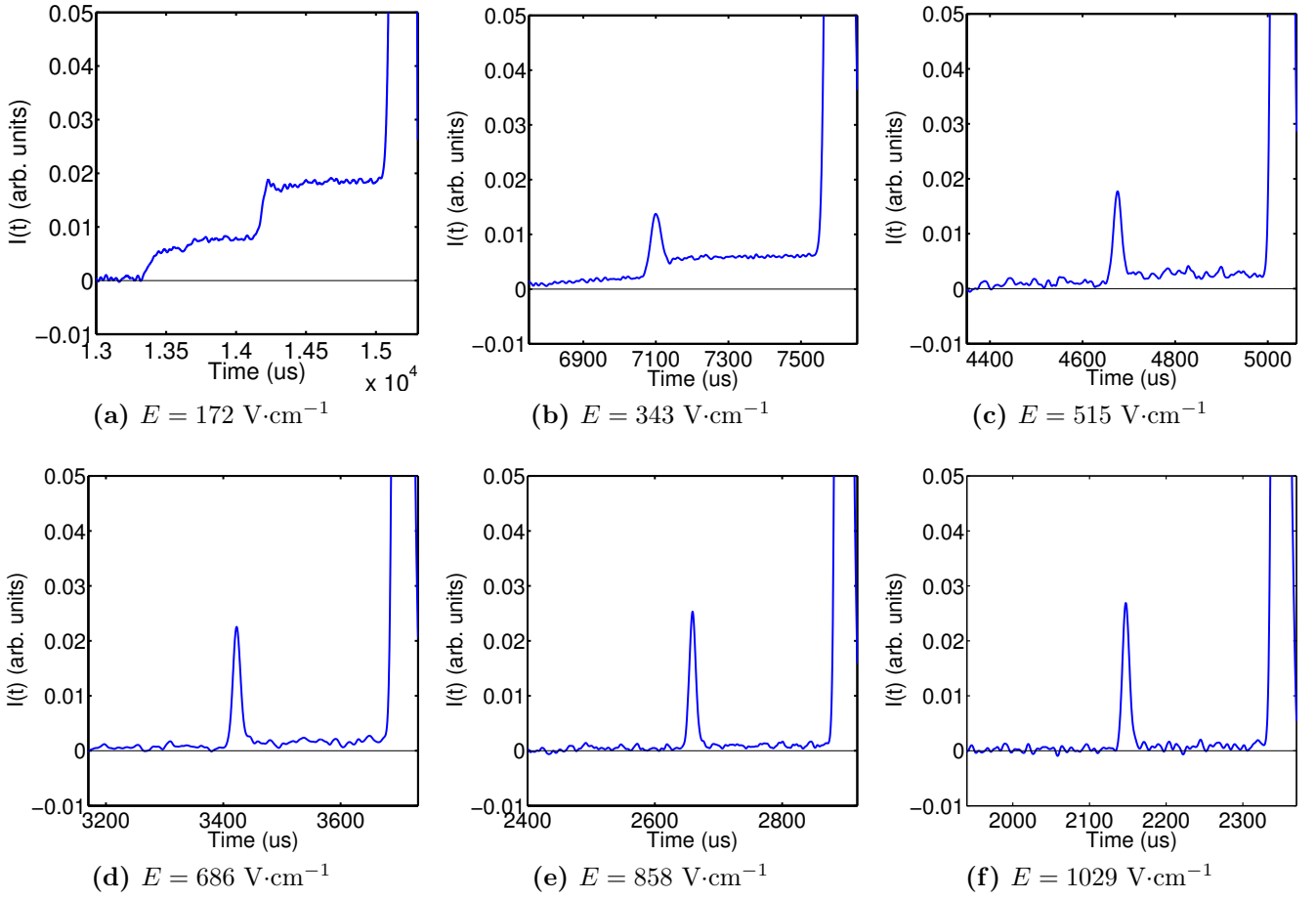


Figure 3: (a)-(f) The zoomed in views of the waveforms from Figure 2. Charge outside of the peaks appears to decrease with increasing field strength while the SF_5^- peak begins to emerge and grow in amplitude.

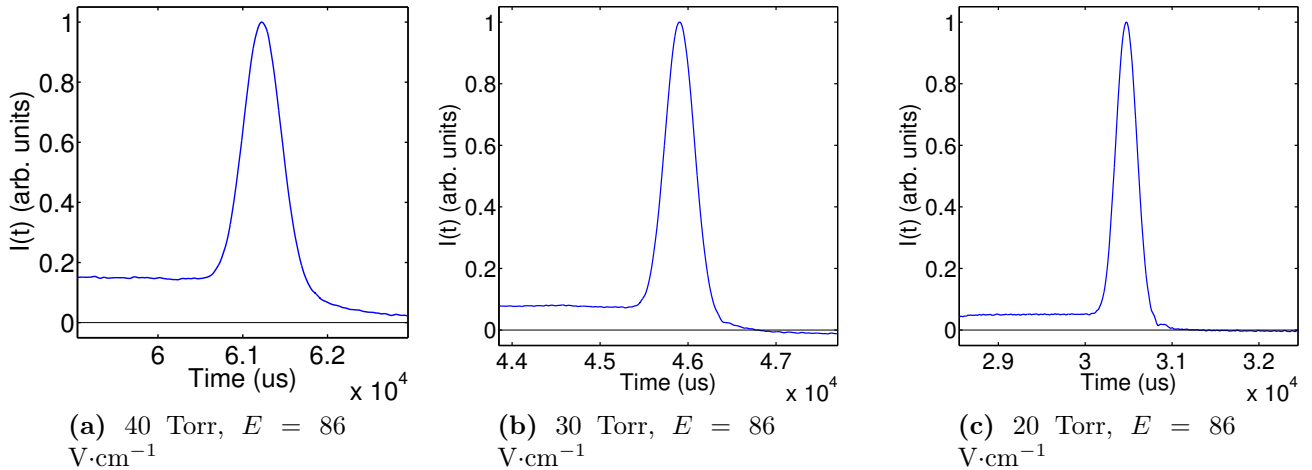


Figure 4: (a)-(c) Average waveforms for 40, 30, and 20 Torr SF_6 at $E = 86 \text{ V}\cdot\text{cm}^{-1}$. Note the long tail on the right side of the peak in (a), which could be due to clustering at low reduced fields in SF_6 .

pressure is reduced, similar to what is observed with increasing drift field at fixed pressure. This anti-correlation between the pressure and drift field would imply a reduced field (E/p or E/N) dependence, but a detailed look at the data does not support this. Comparing the waveforms in Figure 3c and Figure 5b (blue curve), both at the same reduced field but different E and p , we see clear differences in the amount of charge in the non-peak region (both waveforms are normalized with the SF_6^- peak amplitude set to one).

Two other notable features seen on the right side of the SF_6^- peak are the small negative amplitude dip and the long tail at low E/p . As discussed in Section 3.2, the latter could be due to $\text{SF}_6^-(\text{SF}_6)_n$ and $\text{SF}_5^-(\text{SF}_6)_n$ clusters that drift at a slower speed than the SF_6^- anion. The production and drift of $\text{SF}_6^-(\text{H}_2\text{O})_n$ clusters, which is discussed in Section 3.3, could also contribute to this tail. But at higher reduced fields, the formation of such weakly bound clusters should be suppressed, which is supported by our higher E/p data (Figures 4b and 4c). The second feature, the negative amplitude dip, is due to how the THGEM surfaces were electrically connected. The surface facing the cathode was grounded to the aluminum anode end-cap, while the other readout surface is at positive high voltage. As a result, the motion of the positive ions in the avalanche away from the readout induces a small positive signal, then the negative dip occurs as they approach the ground, which is capacitively coupled to the readout surface.

3.3 Water vapor contamination

The relative contribution of the broad component to the waveform discussed above (Figures 2, 3 and 4) was found to depend on the length of the pump-out period prior to operation, and the subsequent rate of out-gassing as monitored with the baratron. Given the propensity for plastics to absorb water vapor and O_2 , the acrylic TPC vessel was an obvious source of contamination. After numerous tests, which included separately adding small quantities of O_2 and water vapor into SF_6 , we confirmed that the broad component was due to H_2O .

To reduce the out-gassing rate and dilute the concentration of contaminants, a long pump-down period (several days) followed by the flushing procedure outlined in Section 2.3 was performed. This greatly reduced the water vapor contamination whose relative effect on the waveforms is shown in Figure 5 for several different reduced fields. These plots show that the effect of water vapor on the waveform is large at low reduced fields (Figure 5a), but subsides significantly at a higher reduced fields (Figure 5c) where it is only at the percent level in the high

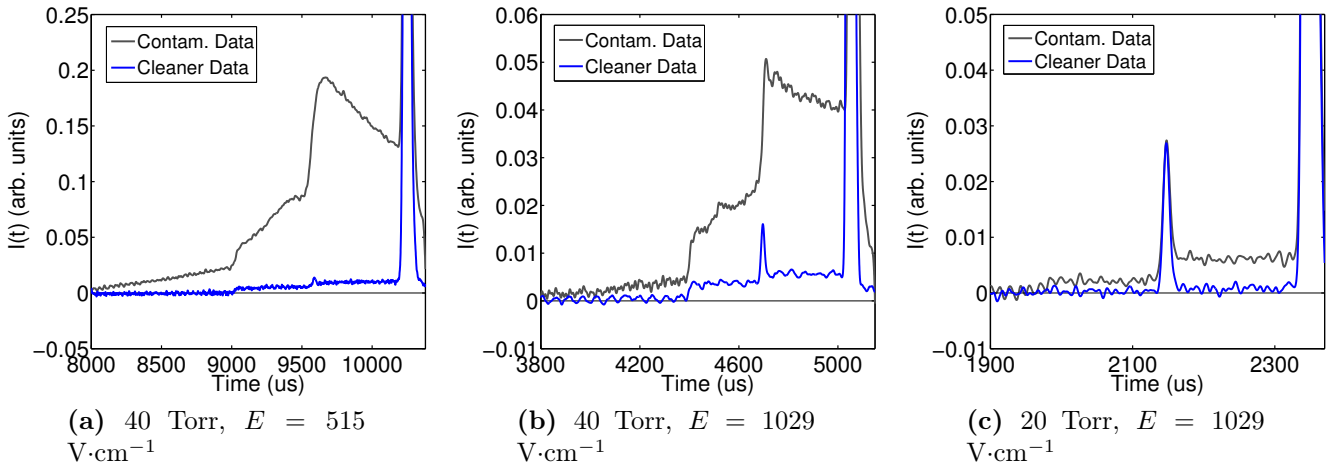


Figure 5: (a)-(c) Comparison of waveform shapes for data with higher (gray) and lower (blue) levels of water vapor contamination at several different reduced fields. The primary SF_6^- peak (outside the vertical range of the plots) has been normalized to 1 in every case. The effect can be considerable ($\sim 20\%$) at lower reduced fields (a) but appears to diminish at a higher reduced field (c).

contamination data. We can place an upper bound on the amount of water vapor contamination in these data using observations of the long term out-gassing rate. By attributing the pressure rate-of-rise entirely to the out-gassing of water vapor, we estimate that the amount in the more contaminated data (gray waveforms in Figure 5) was $<1 \times 10^{-1}$ Torr. In the cleaner data (blue curves in Figure 5), where the detector had a much longer pump down period, we estimate that the amount of water vapor was $<2 \times 10^{-3}$ Torr. The additional step of flushing the vessel twice with SF_6 gas was also undertaken prior to data taking for the cleaner data.

While the effect of water vapor is quite significant, the physical mechanisms responsible for the observed features and their dependence on the reduced field are not fully understood. Previous studies of electron attachment to water have shown that the single molecule does not have a negative ion state [55], so it is unlikely that reactions of H_2O molecules with the primary electrons produced at the cathode are involved. However, electron binding can occur in clusters of water molecules $(\text{H}_2\text{O})_n^-$, where cluster sizes with $n \geq 2$ have been observed [56]. Given the high electron affinity of SF_6 and the extremely low H_2O concentration, even in the high contamination data, the probability of such clusters forming at the primary ionization site should be low.

Stable $\text{SF}_6^-(\text{H}_2\text{O})_n$ clusters, with $n = 1 - 3$, are also known to form [57, 58, 59], thus a more likely scenario is one where water molecules interact directly with SF_6^- anions that are drifting towards the anode³. Because these clusters drift slower than SF_6^- , they cannot account for the broad component in the waveform, but they can undergo further reactions with H_2O , producing the negative ions SOF_4^- and $\text{F}^-(\text{HF})_2$ with a relative probability of 4:1 [59]. If these ions drift faster than SF_6^- , as argued below, they could be responsible for much of the broad component observed in our waveforms.

With this brief overview of the chemistry of SF_6^- in water vapor we can describe how some of the key features arise in the waveforms observed in our experiments. The first is the evolution of the broad component of the waveform, which subsides with increasing E/p , essentially disappearing at the highest reduced fields in our measurements (e.g., Figures 3, 5). This indicates

³ $\text{SF}_5^-(\text{H}_2\text{O})_n$ clusters should also be produced, however, we ignore them and their reactions here, because SF_5^- is only produced at a few percent in our experiment (Figure 3).

that the cluster mediated reactions converting SF_6^- into SOF_4^- and $\text{F}^-(\text{HF})_2$ become suppressed at higher E/p . In our model these reactions require the stable formation and survival of the $\text{SF}_6^-(\text{H}_2\text{O})_n$ clusters, which are weakly held together by hydrogen bonds that are unlikely to survive at high E/p . Without these clusters the pathway to subsequent reactions is closed, leaving only SF_6^- and SF_5^- as observed.

Focusing on the low E/p data where the effects of water vapor are most prominent, we expand our model to explain some of the key features in the waveforms. In our description of SF_6^- and its interactions with water vapor as many as four species can be involved in transporting a negative ion from the cathode to the anode. The drift velocity of this ion will therefore be a weighted average of each species', with the weighting determined by where exactly the conversion from SF_6^- to $\text{SF}_6^-(\text{H}_2\text{O})_n$, and $\text{SF}_6^-(\text{H}_2\text{O})_n$ to either SOF_4^- or $\text{F}^-(\text{HF})_2$ occurs. That the broad component of the waveform extends from the SF_6^- peak down below the SF_5^- means that the SOF_4^- and $\text{F}^-(\text{HF})_2$, and any other cluster mediated reaction products, travel faster than SF_6^- , with some even faster than SF_5^- . Although we have no data on their mobilities in SF_6 , this is reasonable given that both SOF_4^- and $\text{F}^-(\text{HF})_2$ are lighter than SF_6^- . If we assume such a correlation between molecular mass and drift velocity (see Equation 12), then $\text{F}^-(\text{HF})_2$ would have the highest drift velocity, followed by SF_5^- , SOF_4^- and SF_6^- , in that order.

Adopting this assumption we can explain two prominent features in the high contamination waveforms at low E/p , the steps in amplitude at $\sim 4400 \mu\text{s}$ and $\sim 4700 \mu\text{s}$ in Figure 5b. In our model, the former is essentially the shortest drift time in the waveform, which should correspond to $\text{F}^-(\text{HF})_2$ being produced close to the cathode and traveling the full length of the detector. Similarly, the second step at $\sim 4700 \mu\text{s}$ should correspond to the next shortest drift time, that of SOF_4^- . The fact that this step coincides with the SF_5^- peak (Figure 5b, blue curve) agrees with our assumption that two species having similar masses should have similar drift speeds.

Summarizing then, our model predicts that the charge in the region (region 1) between the SF_6^- peak and the step at $\sim 4700 \mu\text{s}$ should consist of a mixture of SOF_4^- and $\text{F}^-(\text{HF})_2$, while in the region (region 2) between $\sim 4700 \mu\text{s}$ and $\sim 4400 \mu\text{s}$ it should be solely due to $\text{F}^-(\text{HF})_2$. That the charge in region 1 is much larger than in region 2 is expected because, as noted above, SOF_4^- and $\text{F}^-(\text{HF})_2$ are produced in the ratio 4:1.

A more detailed analysis of the rich structure observed in the waveforms of the high contamination data is beyond the scope of this paper, nor is it relevant for the goals of directional dark matter detection. For our purposes, the key features of the waveform are the SF_5^- and SF_6^- peaks and their properties, and the remainder of this work will describe their application to directional dark matter searches. The data used in the following sections was taken with a minimum water contamination, similar to the the clean data acquired using the techniques described above (Figures 3 and 5).

In hindsight, our acrylic-based TPC detector, which was designed for high reduced field operation, was not an ideal choice for operating with SF_6 due to its permeability to water vapor and high out-gassing rate. Moreover, this concern extends well beyond acrylic and encompasses a broad collection of polymer-based materials that are hygroscopic. If plastics cannot be avoided, for example because of their desired low radioactivity, then care should be taken to minimize any water vapor contamination during detector construction and data acquisition. Besides the techniques used here to achieve this, we have also considered the use of desiccant and gas recirculating and purification as commonly done in TPCs.

3.4 Relative peak charge and amplitude

With the preceding discussion of the global features of the SF_6 waveform, we now turn our focus to the SF_5^- peak. The importance of detecting both SF_5^- and SF_6^- peaks is that they enable the ability to fiducialize events along the drift direction in the TPC. This provides a powerful tool for rejecting backgrounds in the type of rare searches of interest here, as discussed further

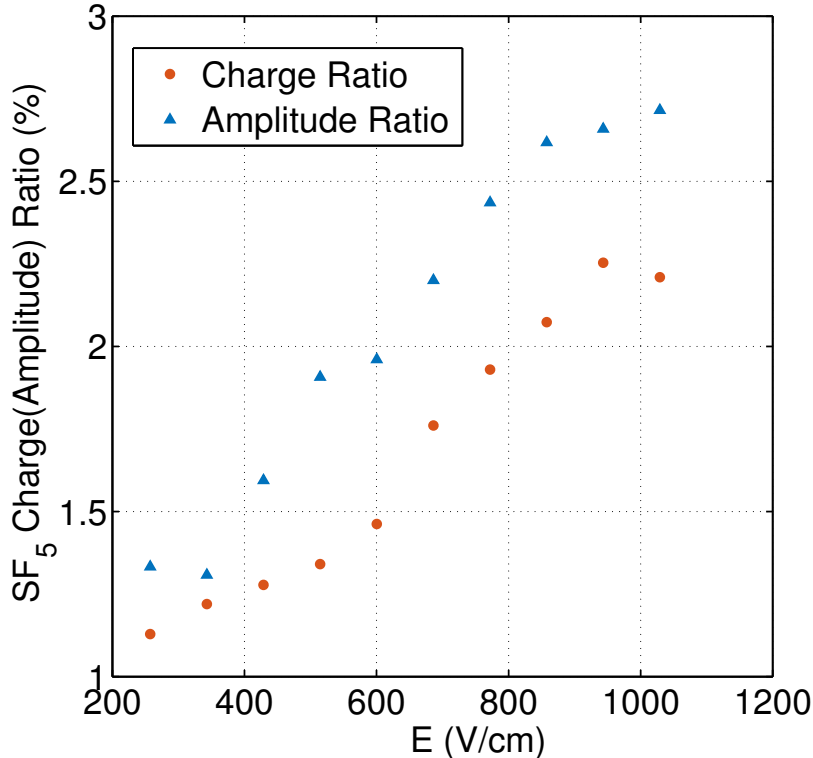


Figure 6: The detected charge and amplitude of the SF_5^- peak relative to SF_6^- in 20 Torr as a function of the electric field. Both quantities increase with electric field but then appear to taper off at a field strength of $\sim 900 \text{ V}\cdot\text{cm}^{-1}$. It is important to note, as discussed in the text, that these are detected quantities and not necessarily the relative amounts produced in the detection volume.

in Section 7 where fiducialization is demonstrated using this tool.

To study the behavior of the secondary SF_5^- peak with field strength, an average of a thousand waveforms was made for each of ten different electric field strengths between $257\text{-}1029 \text{ V}\cdot\text{cm}^{-1}$, all at fixed $p = 20 \text{ Torr}$. From these averaged waveforms, the amplitudes of the SF_5^- and SF_6^- peaks and the amount of charge contained within the peaks was computed. The evolution of the fraction of charge in the SF_5^- peak and its amplitude relative to the SF_6^- peak as a function of the electric field are shown in Figure 6. Both the relative charge and amplitude rise with increasing field strength but then appear to taper off at a field strength of $\sim 900 \text{ V}\cdot\text{cm}^{-1}$ ($E/p = 45 \text{ V cm}^{-1} \text{ Torr}^{-1}$).

The amplitude(charge) of the SF_5^- peak measured at the highest reduced field ($20 \text{ Torr}/1029 \text{ V cm}^{-1} = 158 \text{ Td}$) is $\sim 2.8\%$ (2.2%) that of SF_6^- , which is what their relative capture cross-sections at an electron energy of $\sim 0.1 \text{ eV}$ would predict. It is important to note that this is the *detected* ratio of SF_5^- to SF_6^- and is likely to be lower than what was produced at the site of ionization. This is because of the higher electron affinity of SF_5^- ($2.7 - 3.7 \text{ eV}$), which could lead to a lower gas gain relative to SF_6^- due to the greater difficulty in stripping the electron in the THGEM.

As the detectability of the small SF_5^- peak is critical for fiducialization, it will require high signal-to-noise as well as investigation into possible methods to enhance it. For example, the ratio of SF_5^- to SF_6^- is known to rise at higher electron energies and gas temperatures, with reports indicating that it can exceed 39% at 593 K [4]. This is further discussed in Section 7.2.

4 Reduced mobility

The drift velocities of SF_6^- and SF_5^- were determined by measuring the time difference between the creation of photoelectrons at the cathode using the N_2 laser, and the arrival of ionization at the THGEM corresponding to the respective peaks. The 3.5 ns laser pulses generated what are essentially point-like ionization events in the longitudinal extent. The laser pulse also provided the trigger to the DAQ system and gave us the initial time marker, T_0 . We define the drift time as the time between the initial laser trigger and the arrival time of the pulse peak, T_p , rather than the leading edge of the ionization signal at the THGEM. The magnitude of the drift velocity, v_d , is then given by

$$v_d = \frac{L}{T_p - T_0}, \quad (9)$$

where, $L = 583 \pm 0.5$ mm, is the distance between the THGEM and the cathode. We measured the drift velocity over a range of electric field values ($86 - 1029$ V $\cdot\text{cm}^{-1}$) and pressures (20, 30, 40 Torr). Following convention, we report the mobilities instead of drift velocities.

The mobility, μ , of a drifting ion at a specific gas density is related to the drift speed, v_d , and electric field, E , through the relation:

$$v_d = \mu \cdot E. \quad (10)$$

A standardized quantity called the reduced mobility, μ_0 , is derived from the measured mobility by the expression:

$$\mu_0 = \frac{v_d N}{E N_0}, \quad (11)$$

where $N_0 = 2.687 \times 10^{19}$ cm $^{-3}$ is the gas density at STP (0°C and 760 Torr) and N is the detector gas density at the time of measurement.

Our measured mobilities for CS_2^- , SF_5^- and SF_6^- are plotted in Figure 7 as a function of the reduced field, E/N , in units of the Townsend⁴. We find good agreement between our results for the reduced mobility of CS_2^- in CS_2 and those reported by Ref. [60] in the low field regime (< 50 Td), where our data overlap. Our measurement of the reduced mobility of SF_6^- in SF_6 , extrapolated to zero field, is $\mu_0(\text{SF}_6^-) = 0.540 \pm 0.002$ cm $^2\text{V}^{-1}\text{s}^{-1}$, which agrees well with the result from Ref. [49]. There is also excellent agreement over the full range of reduced fields between our dataset for SF_5^- and SF_6^- mobilities in SF_6 with the mass-identified measurements reported in Ref. [49]. A comparison with other data-sets from Ref. [48] and [50], a majority of which do not have mass analysis, shows agreement over some ranges of reduced fields only.

The CS_2^- mobility is about 13.1% lower than the SF_6^- mobility at 13 Td, but this difference rises to about 17.0% at 158 Td which shows that SF_6^- mobility increases more rapidly with reduced field than CS_2^- mobility. This is unexpected, and goes against our assumptions in Section 3.3, because SF_6 is a much heavier molecule than CS_2 and the drift velocity for ions with mass, m , drifting in a gas with molecules of mass, M , is given by

$$v_d = \left(\frac{1}{m} + \frac{1}{M} \right)^{1/2} \left(\frac{1}{3kT} \right)^{1/2} \frac{eE}{N\sigma}, \quad (12)$$

where σ is the ion-gas molecule cross-section [61]. This implies that the cross-section for $\text{SF}_6^-:\text{SF}_6$ interaction is smaller than, and changes faster with increasing field strength than that for the $\text{CS}_2^-:\text{CS}_2$ interaction. A similar comparison between SF_5^- and SF_6^- shows that the mobility of the former is 6.9% higher than the latter's at about 39 Td, and is 9.3% larger at 158 Td. Note also that transport processes are also energy dependent as can be seen with the rise in mobility with increasing reduced field for all of the negative ion mobilities shown in Figure 7. This has important implications for diffusion at the higher reduced fields, as shown in the next section.

⁴1 Td = 10^{-17} V cm 2 , 1 V cm $^{-1}$ Torr $^{-1}$ = 3.066 Td at $T = 296$ K.

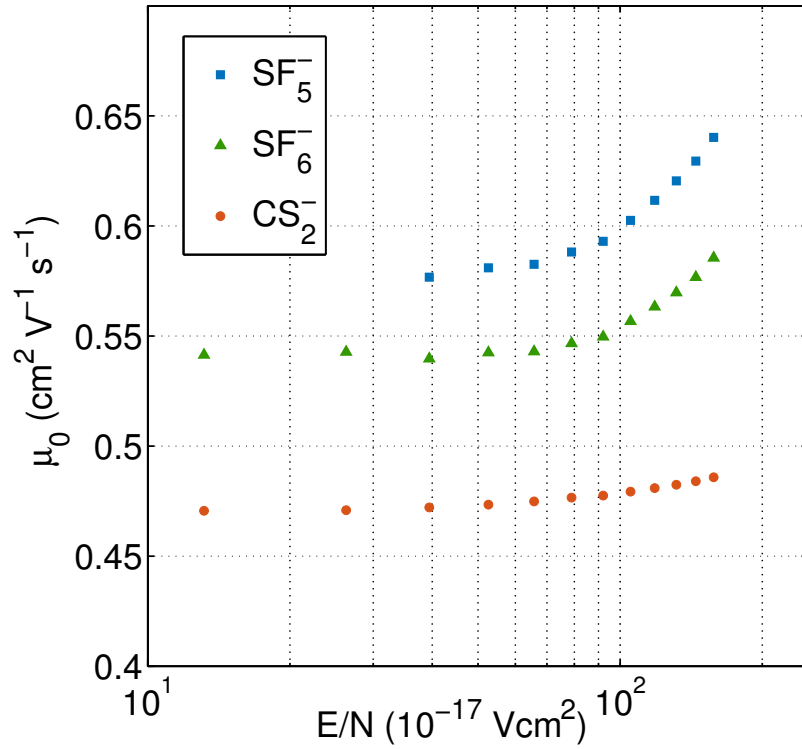


Figure 7: The reduced mobility as a function of reduced field for SF_5^- and SF_6^- in SF_6 and CS_2^- in CS_2 . The SF_5^- mobilities only go down to about 40 Td below which its peak becomes difficult to identify. Our results for SF_5^- and SF_6^- are in excellent agreement with those found in Ref. [49] while the CS_2^- results agree with those from Ref. [60]. The combined uncertainty due to instrumental precision is 1%.

5 Longitudinal diffusion

At low field strengths where the drifting charge cloud has thermal energy, the diffusion coefficient can be approximated by its zero reduced field limit, $D(0)$ ⁵. This is related to the mobility and gas temperature through the Nernst-Townsend-Einstein relation:

$$\frac{D(0)}{\mu(0)} = \frac{kT}{e}, \quad (13)$$

where e is the ion charge [62]. At higher field strengths, diffusion can enter the non-thermal regime where it is given approximately by the generalized Einstein relations [63]. These predict that deviations from $D(0)$ will occur when the field derivative of the reduced mobility becomes non-zero, which, according to the data shown in Figure 7, is expected for $E/N \sim 60 - 70$ Td for SF_6^- . In the non-thermal regime, the deviations in longitudinal diffusion, D_L , are proportional to this derivative and larger than those in transverse diffusion, D_T . In this work we only measure longitudinal diffusion and, by comparing it with the predictions of Equation 13, look for deviations from the thermal limit.

From Equation 13, a starting point-like charge cloud drifting over a distance, L , has a longitudinal diffusion width, σ_z , given by

$$\sigma_z^2 = 2D_L t = \frac{4\epsilon L}{3eE} = \frac{2kTL}{eE}, \quad (14)$$

where $t = L/v_d$ and $\epsilon = 3/2kT$ [61]. As our measurements are of pulse widths, we relate the diffusion in the time domain, σ_t , to σ_z using the drift velocity:

$$\sigma_z = \sigma_t \cdot v_d. \quad (15)$$

Customarily, diffusion is expressed by normalizing the measured value relative to the drift length:

$$\sigma_0 = \frac{\sigma_z}{\sqrt{L}} = \sqrt{\frac{2kT}{eE}}, \quad (16)$$

where σ_0 is typically expressed in units of $\mu\text{m}/\sqrt{\text{cm}}$.

The pulses used to measure diffusion of SF_5^- and SF_6^- were obtained from waveforms generated using ionization produced at the cathode, a known $L = 58.3$ cm drift distance, with the N_2 laser as described in Section 2.2. One thousand of these waveforms were averaged together at each pressure and electric field to increase signal-to-noise, resulting in the averaged waveforms shown in Figures 2, 3 and 4. As the SF_5^- or SF_6^- pulses are not strictly Gaussian, some care was required in extracting their widths. The main contribution to their non-Gaussianity is from the positive ion tail on the right side, whose origin was explained in Section 3.2. To minimize its effect, only a fraction of the left hand side of the waveform above 10% of the peak was used to fit to a Gaussian curve. This fraction was determined iteratively by modeling the relative contributions of the collected charge signal and the positive ion induced signal to the pulse amplitude. Additionally, due to the broad structure from residual water vapor contamination at low reduced field (Section 3.2), only data with $E > 171$ $\text{V}\cdot\text{cm}^{-1}$ at 20 Torr and $E > 257$ $\text{V}\cdot\text{cm}^{-1}$ at 30 and 40 Torr were used.

Using this procedure we found σ_{fit} , which is mostly due to diffusion with small contributions from other effects. The latter are the smoothing time, σ_{smooth} , laser spot size, σ_{spot} , the spread in the electron-capture length, σ_{capture} , and effects at the THGEM, σ_{THGEM} . We have no direct measurements of σ_{capture} or σ_{THGEM} , so we make no attempt to correct for them here. In our

⁵In this regime the charge cloud diffuses isotropically, so the longitudinal and transverse components, D_L and D_T , are the same and equal to $D(0)$.

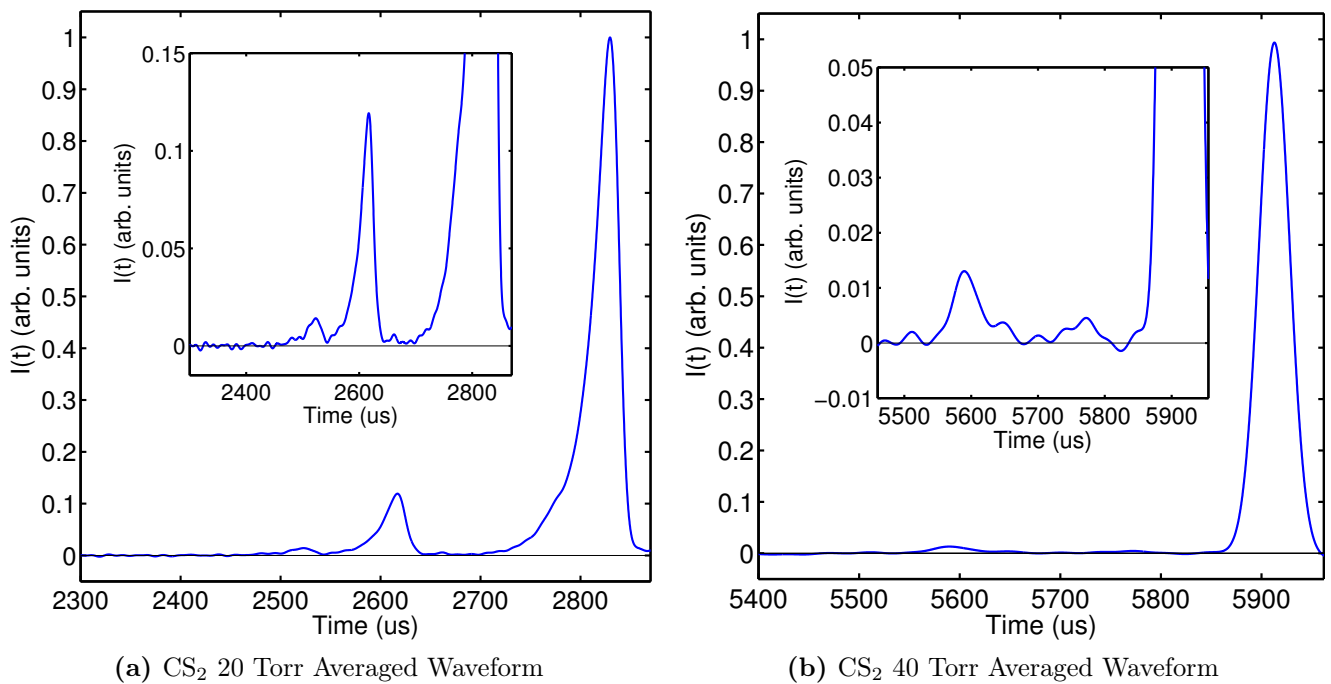


Figure 8: (a) The averaged waveform for 20 Torr CS₂ at $E = 1029 \text{ V}\cdot\text{cm}^{-1}$ showing the presence of a large secondary peak at $\sim 2600 \mu\text{s}$ and the possible appearance of two additional peaks at $\sim 2660 \mu\text{s}$ and $\sim 2520 \mu\text{s}$ (inset). In addition, the distortion in the waveform shape is clearly seen in both the primary and secondary peaks at this high reduced field. This behavior is not observed in the SF₆ waveforms at high reduced fields. (b) The average waveform for 40 Torr CS₂ at $E = 1029 \text{ V}\cdot\text{cm}^{-1}$ which shows no clear secondary peaks or distortion in waveform shape.

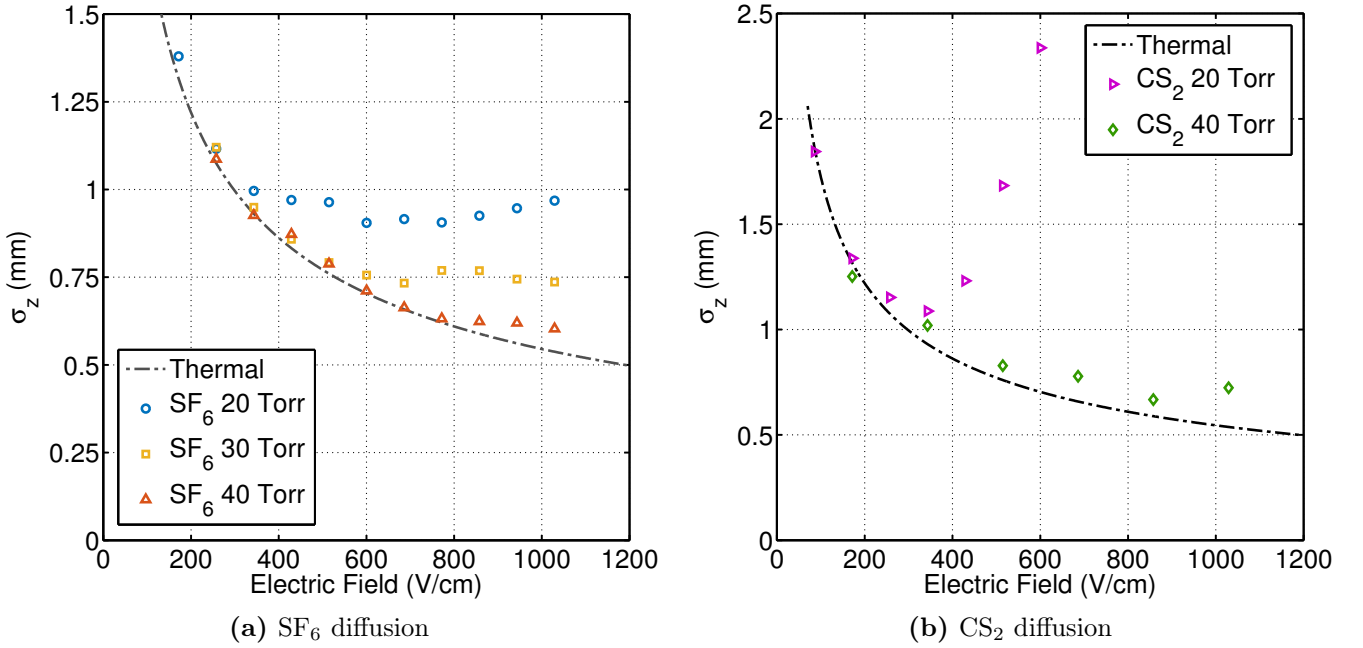


Figure 9: (a) The longitudinal diffusion, σ_z , for 20, 30, and 40 Torr SF₆ as a function of electric field for a drift length of 58.3 cm. The plotted quantity includes the broadening effects of the finite THGEM hole pitch as well as the capture process. The dot-dashed line shows the predicted width for thermal diffusion from Equation 14. For the 40 Torr data, the measured width begins to deviate away from the thermal prediction at $\sim 800 \text{ V}\cdot\text{cm}^{-1}$. Similarly for the 30 Torr and 20 Torr data, deviations from thermal diffusion occur at $\sim 600 \text{ V}\cdot\text{cm}^{-1}$ and $400 \text{ V}\cdot\text{cm}^{-1}$, respectively. (b) The fitted pulse width for 20 and 40 Torr CS₂. At 20 Torr the pulse width begins to deviate considerably from thermal at $\sim 400 \text{ V}\cdot\text{cm}^{-1}$. The corresponding distortion seen in the waveform in Figure 8a could, however, also be due to a longer electron capture mean-free-path at high E/p (refer to the text).

measurements, the laser spot size contribution to the longitudinal width is negligible, so we set $\sigma_{\text{spot}} \sim 0$. Thus, assuming no correlation, we subtract σ_{smooth} from σ_{fit} in quadrature to get the diffusion width in time:

$$\sigma_t = \sqrt{\sigma_{\text{fit}}^2 - \sigma_{\text{smooth}}^2}. \quad (17)$$

Using Equation 15, we finally get σ_z , the longitudinal spread of the charge distribution in space due to diffusion. The systematics on σ_z , mainly due to not accounting for σ_{capture} and σ_{THGEM} , are briefly discussed below.

The same fitting procedure was applied to our CS₂ data taken at 20 Torr (Figure 8a) and 40 Torr (Figure 8b). The 20 Torr, high reduced field waveform shown in Figure 8a appears distorted on the left and has at least one additional secondary peak at $\sim 2600 \mu\text{s}$. These features are discussed in Section 5.4.

5.1 σ_z results

In Figure 9, the longitudinal diffusion, σ_z , is plotted as a function of electric field for 20, 30, and 40 Torr SF₆ and 20 and 40 Torr CS₂ data. Overlaid are curves for thermal diffusion calculated using Equation 14. In the 40 Torr SF₆ data, σ_z begins to deviate from the thermal prediction at around $800 \text{ V}\cdot\text{cm}^{-1}$. Similarly, in the 30 Torr and 20 Torr SF₆ data, deviations from thermal diffusion occur at around $600 \text{ V}\cdot\text{cm}^{-1}$ and $400 \text{ V}\cdot\text{cm}^{-1}$, respectively. In terms of the reduced field, the deviations all begin to occur at approximately $E/p = 20 \text{ V}\cdot\text{cm}^{-1}\cdot\text{Torr}$ or $E/N = 60 \text{ Td}$. This is close to our estimate above of $E/N \sim 60 - 70 \text{ Td}$ based on the generalized Einstein relations.

The 40 Torr CS₂ diffusion data shown in Figure 9 indicate a larger systematic than observed for SF₆. This is likely due to a longer mean free path for electron capture and is discussed further below in Section 5.2. Assuming that this systematic is field independent, the data appear to follow thermal diffusion out to $\sim 500 \text{ V}\cdot\text{cm}^{-1}$ (38 Td) and perhaps even to $\sim 800 \text{ V}\cdot\text{cm}^{-1}$ (61 Td). Precision measurements of σ_z [60] have confirmed thermal out to 23 Td and other measurements [?] indicate that the low field approximation applies to CS₂ out to $\sim 42 \text{ Td}$.

At 20 Torr we observe a distortion in the waveform at high reduced fields and one or more smaller peaks begin to appear (Figure 8a), which also grow with E/p . The effect of the distortion on σ_z begins at $\sim 50 \text{ Td}$ and is dramatic as seen in Figure 9. The origin of the distortion could be a deviation from thermal diffusion or a growing inefficiency in electron capture at high E/p , which naturally explains the observed tail on the fast side of the waveform. The fact that the reduced mobility has a weaker dependence on E/p than SF₆⁻ (Figure 7) also points to electron capture. Measurements of the lateral diffusion should help determine which of these effects dominates. The secondary features are discussed in Section 5.4.

5.2 Systematics on σ_z

Here we place bounds on the two primary sources of systematics to the measured diffusion width, the spread in the electron-capture mean-free-path and non-uniformity of the electric field near the THGEM. Given how well matched our σ_z values are to the diffusion limit at low reduced fields (Figure 9), any non-diffusion contributions cannot be large. At low reduced fields in 40 Torr CS₂, an upper bound on the spread in capture distance of 0.35 mm was estimated by Ref. [60]. Based on measurements of the attachment cross-section in SF₆, the mean free path for attachment in our experimental apparatus should be of order $\sim 1-10 \mu\text{m}$ and, hence, a negligible contribution to σ_z . The broadening effect due to the non-uniformity in the drift field close to the THGEM should depend on the THGEM pitch, and the fields in the holes and TPC drift region. This can be modeled but we can provide an upper bound estimate based on the low E/p region of the SF₆ data in Figure 9a, where we expect thermal diffusion. The σ_z data in this region are

systematically slightly higher than the thermal prediction, thus, assigning the difference taken in quadrature to the THGEM, gives the upper bound of $\sigma_{\text{THGEM}} < 0.2$ mm.

In 40 Torr CS₂, the systematic differences in the low E/p regime (Figure 9b) are larger than in SF₆, which is probably due to a longer electron capture distance as discussed above. Assuming that the contribution from the THGEM is the same for both gases, $\sigma_{\text{THGEM}} \sim 0.2$ mm, we can assign the remaining difference to the spread in electron capture distance in CS₂. This gives $\sigma_{\text{capture}} \sim 0.3$ mm, which is within the upper bound for CS₂ from Ref. [60] given above. In the 20 Torr CS₂ data we speculate that the large deviation in σ_z from thermal observed above 50 Td is due to inefficient electron capture, rather than diffusion. Measurements of lateral diffusion will help test this hypothesis. A more accurate estimate for the sum total of non-diffusion contributions, including σ_{THGEM} and σ_{capture} , can also be determined by measuring the waveform width as a function of drift distance. This is left for future work.

5.3 Implications for directional searches of low mass WIMPs

For dark matter searches in the low, ~ 10 GeV/ c^2 , WIMP mass regime, the lowest possible energy thresholds are desired. For directional DM searches in low pressure TPCs, as discussed in some detail in Ref. [64], the ability to lower the pressure lengthens the tracks, which, in principle, will lower the *directional* energy threshold. With the assumption that the minimum track length for which directionality can be detected is an invariant, and using data at 100 Torr, Ref. [64] showed that pressures in the range $\sim 5 - 10$ Torr would be optimal for maximizing sensitivity for directional low mass WIMPs searches. This assumption requires that physical effects that could impact track reconstruction, such as diffusion, do not worsen at lower pressures.

In this regard, our measurements of diffusion at 20 Torr for both SF₆ and CS₂ provide an important data point to test this assumption. As discussed above and shown in Figure 9a, deviation from thermal diffusion in our SF₆ data occur at ~ 70 Td at all pressures. At lower pressures, ~ 70 Td corresponds to a lower drift field where thermal diffusion is higher, as can be seen in Figure 9a. Thus, in 20 Torr SF₆ the minimum longitudinal diffusion observed in our data is $\sigma_z \sim 0.9$ mm, quite a bit higher than the $\sigma_z \sim 0.63$ mm in 40 Torr. This means that the minimum track length with directionality is about 1.5 times longer at 20 Torr than at 40 Torr. If the trend we observe continues at lower, 10 – 15 Torr pressures, it may impose a fundamental limit on the directional energy threshold imposed by diffusion.

For CS₂, the data at 20 Torr shown in Figures 8a and 9b are difficult to interpret from the diffusion perspective. As discussed above, the long tail on the fast side of the waveform is characteristic of electron capture mean free path, but this requires confirmation. This hypothesis is nevertheless supported by the mobility data of Figure 7, which suggests that diffusion in CS₂ is deviating less from thermal, and at higher reduced fields, than SF₆.

It is clear that further detailed studies of diffusion for both CS₂ and SF₆ are needed to settle these questions. These should include measurements of the transverse component, and estimates of the systematics, which, together with the measurements in this work will provide better constraints on the possibility of directional low mass WIMP searches.

Nevertheless, the current data can be used to provide a reasonable estimation of the behavior of the tracking resolution with pressure. At low reduced fields, the tracking resolution defined as, $M \equiv \sigma(E)/R \propto \sigma(E) \cdot p$, is inversely proportional to the track range, R , and proportional to the pressure, p . Thus, M is defined as the minimum resolvable track range and reducing the pressure by a factor of two will improve the resolution by the same factor. However, at high reduced fields the scaling no longer holds because to stay within the thermal limit the electric field must also be reduced by the same factor to keep E/p constant and below the critical non-thermal reduced field. Because $\sigma \propto 1/\sqrt{E}$, lowering E raises the diffusion by the square root of the reduction factor. Hence, the best attainable resolution at a given pressure will improve by $\sqrt{f_p}$, where $f_p = p_1/p_2$ is the pressure reduction factor. Of course, this is only an approximate

relation because from Figure 9a, the diffusion does, in fact, decrease slightly or remains constant for electric fields beyond the critical value where a deviation from thermal behavior is observed. Nevertheless, the approximate relation provides a reasonable estimation for the best attainable resolution at a given gas pressure. But even this approximate scaling will eventually break down at very low pressures as the electron capture length becomes a significant contribution to a diffusive-like spread in the track. The behavior of σ_z in 20 Torr CS₂ indicates this eventual outcome.

5.4 Secondary peak in CS₂

Finally, we return to the small, secondary peak observed in the 20 Torr CS₂ data shown in Figure 8a. This feature first appears at a drift field of $E = 343 \text{ V}\cdot\text{cm}^{-1}$ at 20 Torr CS₂ and has a drift speed that is $\sim 6.2\%$ faster than, and an amplitude only 0.4% that of the primary peak. When the drift field is increased to $E = 686 \text{ V}\cdot\text{cm}^{-1}$, the secondary peak's drift speed and amplitude increase to 6.8% and 4.6% , respectively, relative to that of the primary peak. Finally, at $E = 1029 \text{ V}\cdot\text{cm}^{-1}$, the secondary peak is about 7.5% faster than the primary while its amplitude continues to grow and reaches about 11.7% of the primary's peak value (Figure 8a). In the 40 Torr CS₂ data there is a hint of a secondary peak at the highest field, $E = 1029 \text{ V}\cdot\text{cm}^{-1}$, which is a factor of ~ 10 lower in amplitude than the main secondary peak seen at 20 Torr.

Additional negative ion species have been observed in CS₂ gas mixtures when a small amount of O₂ is added [19]. In Ref. [19], at least three additional negative ion species (minority peaks) were reported, all with higher mobilities than CS₂, and peak amplitudes that grow, relative to the main CS₂⁻ peak, with the O₂ fraction. The amplitude of the largest of these three peaks is approximately a factor $2\times$ larger than the next highest, and this ratio is maintained independent of the O₂ fraction or drift field, up to $E = 580 \text{ V}\cdot\text{cm}^{-1}$ [19, 17]. The only variable that affects the relative amplitudes appears to be the drift distance; increasing this lowers the amplitude of the middle peak. To date, the physical mechanism behind the minority peaks in the CS₂/O₂ mixture is unknown.

For a number of reasons, the secondary peak seen in our 20 Torr CS₂ data is unlikely to be one of the minority peaks due to O₂ contamination: we see only one peak whereas three should clearly be visible; our secondary peak's amplitude increases by an order of magnitude with E from $343 \text{ V}\cdot\text{cm}^{-1}$ to $686 \text{ V}\cdot\text{cm}^{-1}$, but no significant variation in the minority peak amplitudes was observed over the range $E \sim 270 - 580 \text{ V}\cdot\text{cm}^{-1}$ in Ref. [19]; a secondary peak is barely visible in our 40 Torr data, which was acquired in similar conditions to the 20 Torr data.

We also note that although our acrylic TPC was a source of water vapor from out-gassing, as discussed in Section 3.3, the permeability coefficient of water vapor in acrylic is over three orders of magnitude larger than for O₂. Thus, the level of O₂ is probably too low to affect our data at the level seen in Figure 8a, which given all the other inconsistencies of this hypothesis, indicates a different origin for the small peak.

A more likely hypothesis is that the peak is due to S⁻ or CS⁻, which are known products of the auto-dissociation of CS₂^{-*} [65, 66], similar to how SF₅⁻ is produced via Equation 5. The cross-sections for both S⁻ and CS⁻ production via this mechanism are non-zero at zero electron energy and peak at 0.5 eV and 1.2 eV , respectively. The S⁻ peak is narrower and larger by a factor ~ 20 than that for CS⁻. This suggests that our secondary peak is due to S⁻, and also explains its rapid fractional increase with E described above since the S⁻ production cross-section increases with electron energy in the $0 - 0.5 \text{ eV}$ range.

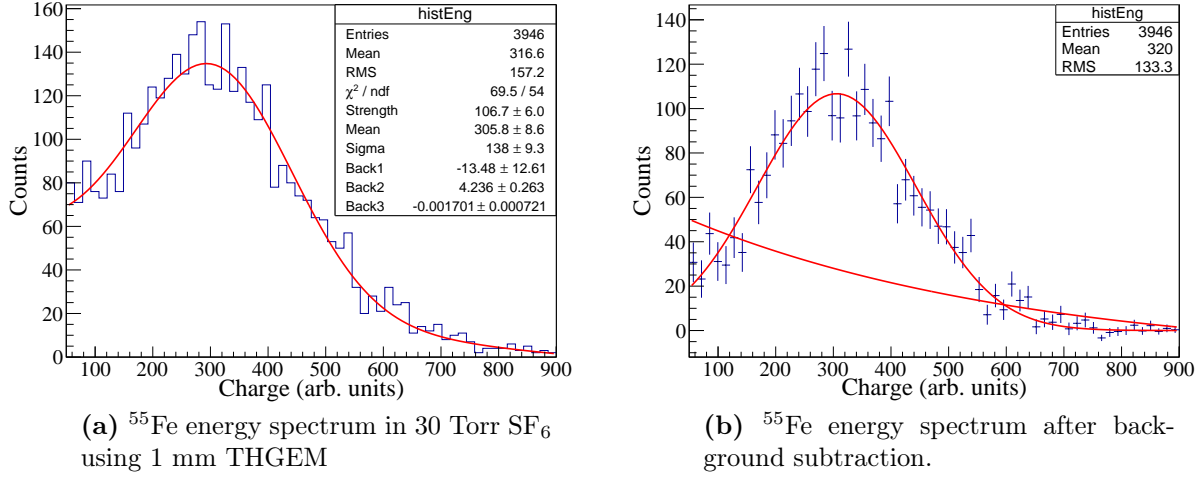


Figure 10

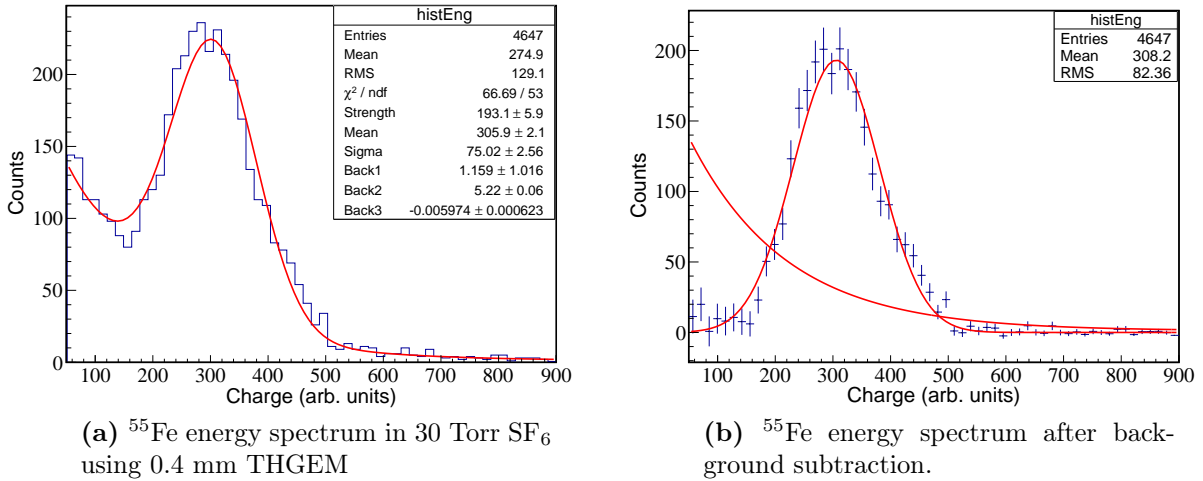


Figure 11

6 Gas gain

Previous works have shown that gas gains greater than 1000 can be achieved in electronegative gases with proportional wires [67], GEMs [68], and bulk Micromegas (Micro Mesh Gaseous Structure) [69]. In contrast to electron gases where only moderate electric fields of order $100 \text{ V}\cdot\text{cm}^{-1}\text{Torr}^{-1}$ are needed to accelerate electrons to energies close to the ionization potential of the gas, electronegative gases require much higher electric fields to initiate avalanche even though the electron affinity is usually much lower than the ionization potential [70]. For CS_2 , measurements show that the minimum reduced field, $(E/p)_{\text{min}}$, needed to initiate avalanche is over one order of magnitude larger than for the electron drift gas P10 (10% methane in argon) [70]. A similar study can be done for SF_6 , but in this section we omit a discussion of the detailed mechanism for avalanche and instead focus on the gas gains.

Two THGEMs of thickness, 0.4 mm and 1 mm were used to achieve gas gain in SF_6 . Other than the thicknesses, the pitch and other THGEM parameters were the same as those described in Section 2.1. To measure the gain an ^{55}Fe 5.89 keV X-ray source was employed. To convert the

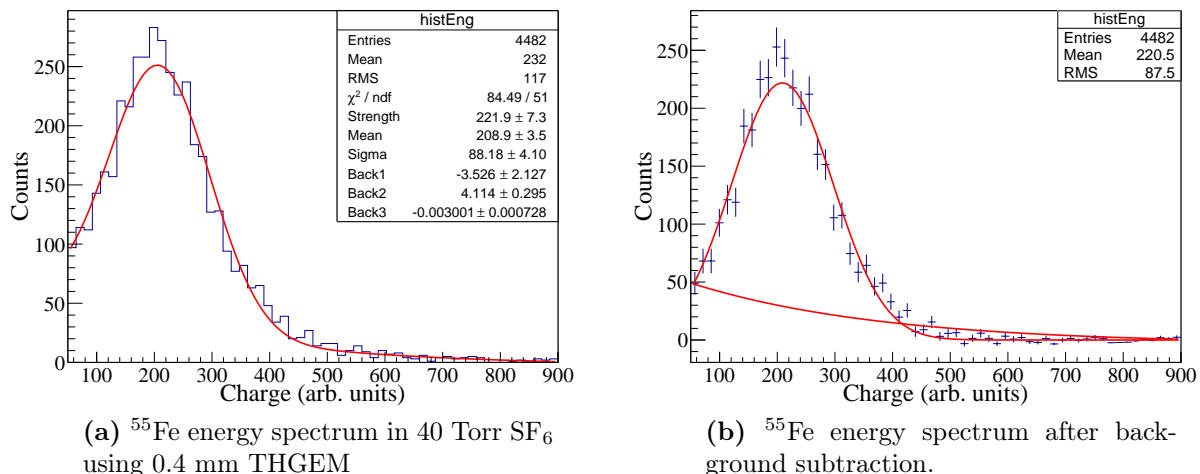


Figure 12

energy of the X-ray into the number of electrons produced during the initial conversion process, we used the W-factor, defined as the mean energy required to create a single electron-ion pair. For SF_6 , this value has been measured using α particles [71] and a ^{60}Co γ source [72], giving $W_\alpha = 35.45$ eV and $W_\gamma = 34.0$ eV, respectively. The slight disagreement is actually consistent with other measurements of W-factors, which find that W_α exceeds $W_{\gamma,\beta}$ for molecular gases [73]. Because we used an X-ray source, we adopt the W-factor from Ref. [72], so the average number of primary electrons, N_p , created by an ^{55}Fe X-ray conversion in SF_6 is

$$N_p = \frac{E_{^{55}\text{Fe}}}{W_\gamma} = \frac{5.89 \text{ keV}}{34.0 \text{ eV}} \simeq 173. \quad (18)$$

The effective gas gain is then given by,

$$G_{\text{eff}} = \frac{N_{\text{tot}}}{N_p}, \quad (19)$$

where N_{tot} is the total number of charges read out with the preamplifier. In general, this is less than the total number of charges produced in the avalanche due to inefficient charge collection, hence, the measured gain is an effective and not an absolute value. In our case, essentially all of the electrons produced in the avalanche were collected, but there was an additional contribution to the pulse from the positive ion induced signal. This systematic was not removed. To determine N_{tot} from the measured voltage pulse, $V(t)$, the standard calibration procedure of injecting a known charge into the preamplifier was used. For this we used an ORTEC 448 Research Pulser to inject charge into the 1 pF calibration capacitor inside the ORTEC 142 preamplifier.

For the gain measurement at each pressure, the THGEM voltage was raised until ^{55}Fe events were visible on the oscilloscope. The voltage ramp continued until energetic sparks were observed and/or until the rate of micro-sparks and background events approached that of the ^{55}Fe source. Figures 10a and 11a show the spectra acquired in 30 Torr SF_6 using a 1 mm and 0.4 mm THGEM, respectively. The spectrum taken with the 1 mm THGEM (Figure 10a) is much broader, indicating a worse energy resolution, than that taken with the 0.4 mm THGEM spectrum (Figure 11a). Figures 12a and 13 show the spectra acquired in 40 Torr and 60 Torr, respectively, both using the 0.4 mm THGEM. For the 60 Torr spectrum the maximum stable gas gain was not sufficient to clearly resolve the peak above background. However, there was a clear rate difference above the trigger threshold when the ^{55}Fe source was switched on and off,

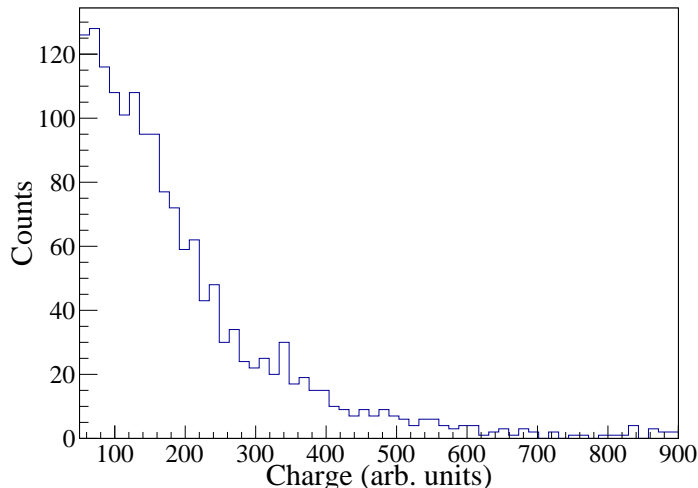


Figure 13: An ^{55}Fe spectrum acquired in 60 Torr SF_6 using a 0.4 mm THGEMs. The peak is not observable due to a combination of low gain and large energy resolution. However, there is a clear rate difference between ^{55}Fe source on versus off, indicating there is indeed sufficient gas gain for detecting these low-energy events.

indicating that the tail of the ^{55}Fe distribution is contained in the spectrum. At 20 and 100 Torr a similar rate difference was observed between source on and off using the 0.4 mm THGEM, but spectra were not acquired due to instability.

None of the spectra are Gaussians, but contain an extra exponential component due to micro-sparks and background events. To better identify the background and signal components and quantify their shapes, the spectra were fit with a Gaussian signal component, and an exponential plus constant for the background component. The fitted total spectrum and the separated signal and background components are shown in Figures 10a and 10b for the 30 Torr data acquired with the 1 mm THGEM. The reduced chi-square (χ^2/ndf) of the fit is 1.29. Similar fits are shown in Figures 11a and 11b for the 30 Torr data, and Figures 12a and 12b for the 40 Torr data, both acquired with the 0.4 mm THGEM. The reduced chi-squares for these fits are 1.26 and 1.66, respectively.

The mean of the Gaussian fit was used to derive the effective gas gain and the width gave the energy resolution, both of which are tabulated in Table 1 for each experimental configuration. Other important parameters that describe the operating conditions for the different gain measurements are also listed there to aid in interpreting our results. Of these, the reduced field inside the THGEM holes, E_h/p , will be most useful in understanding the differences in the energy resolution and gas gains shown in Table 1. The electric field, E_h , in the THGEM was approximated by $\Delta V/d$, where ΔV is the voltage across the THGEM and d is its thickness.

The spectra shown in Figures 10 - 13, with the corresponding gas gains and energy resolutions summarized in Table 1, can be understood with some knowledge of the physical processes governing the avalanche process in negative ion gases. These processes involve stripping the electron from the negative ion, which initiates the avalanche, and the recapture of electrons by SF_6 in the avalanche, both of which can negatively impact gas gain and energy resolution. The stripping will occur at some depth, z , inside the THGEM hole that is determined by the electron detachment mean-free-path, λ_{detach} , a function of the reduced field. A large λ_{detach} , relative to the THGEM thickness, d , will lead to a larger average depth, z , where the avalanche begins, resulting in lower gas gains, larger gain fluctuations, and worse energy resolution.

In addition, the avalanche process in negative ion gases will suffer from a competition with

Table 1: THGEM parameters and results

d (mm)	p (Torr)	ΔV (V)	E_h (kV·cm ⁻¹)	E_h/p (V·cm ⁻¹ Torr ⁻¹)	G_{eff}	σ/\mathcal{E} (%)
0.4	30	820	20.50	683	3000	25
1.0	30	1005	10.05	335	3000	45
0.4	40	880	22.00	550	2000	42
0.4	60	1020	25.50	425	-	-

recapture on the neutral molecule or its fragments produced in the THGEM holes (e.g., by auto-dissociation). In SF₆, although the cross-sections for attachment fall with electron energy, the higher electron energies in the THGEM will favor auto-dissociation to SF₅⁻, SF₄⁻, SF₃⁻ and F⁻⁶, over collisional stabilization to SF₆⁻, and these fragments have higher electron affinities than SF₆⁻ (1.06 eV) [21]. Regardless of the details, if recapture occurs the avalanche is halted momentarily until the electron can be stripped again, which further suppresses the gain and worsens energy resolution. As the cross-sections for attachment, dissociation, and ionization of SF₆ and its fragments depend on the electron energy, the distinctive spectral shapes, energy resolutions, and gas gain must originate from the dependence on the reduced field in the THGEM.

With this overview, we can attempt to understand the spectra shown in Figures 10 - 13 (also refer to Table 1). A comparison of the 30 Torr spectra taken with the 0.4 mm and 1 mm THGEMs shows a factor ~ 2 worse energy resolution in the 1 mm THGEM. This difference is clearly due to the $2\times$ lower reduced field, E_h/p , in the 1 mm THGEM, which, as discussed above, will lead to a larger λ_{detach} and higher probability of recapture, both of which will lead to the large gain fluctuations that result in poor energy resolution. If the 1 mm THGEM could have sustained a larger ΔV , leading to a higher E_h/p in the holes, a potentially much larger gas gain and better energy resolution could have resulted.

Next, we look at the differences between the 30 and 40 Torr spectra, both taken in the 0.4 mm THGEM. The energy resolution in 40 Torr is almost $2\times$ worse, nearly as poor as for the 30 Torr data taken in the 1 mm THGEM. Here again, it is due to the lower reduced field in the 40 Torr case, $E_h/p = 550$ kV·cm⁻¹, relative to that for the 30 Torr case, $E_h/p = 683$ kV·cm⁻¹. The fact that the E_h/p lies closer to the 30 Torr, 0.4 mm case than to the 40 Torr, 1 mm case, indicates that either λ_{detach} or the attachment probability depend strongly on energy. Which of these variables dominates in the effects we see here is not known at this time. We note, however, that although the reduced fields differ, the electric fields are comparable for the two cases, $E_h \sim 20$ kV·cm⁻¹, which supports our claim that the relevant processes are governed by E_h/p .

The low gas gains at the higher 60 – 100 Torr pressures were also due to low E_h/p , which we were unable to sustain at the levels achieved at low pressures. In the 60 Torr 0.4 mm THGEM data, we could only reach $E_h/p = 425$ kV·cm⁻¹, which was insufficient to raise all ⁵⁵Fe events above the trigger threshold. This along with the broadening of the peak at low avalanche reduced field cause the peak in the spectrum to fall below the range shown in Figure 13. Multiple THGEMs should work at higher pressures and other MPGD devices, such as thin GEMs and Micromegas, should be attempted as well. The latter two could also achieve much higher reduced fields, albeit over a shorter avalanche region, which could help with improving the energy resolution. These are interesting questions for future studies.

⁶The electron affinities of SF₅, SF₄, SF₃, and F are 2.7 – 3.7 eV [52], 1.50 eV [75], 1.84 eV [75], and 3.4012 eV [74], respectively.

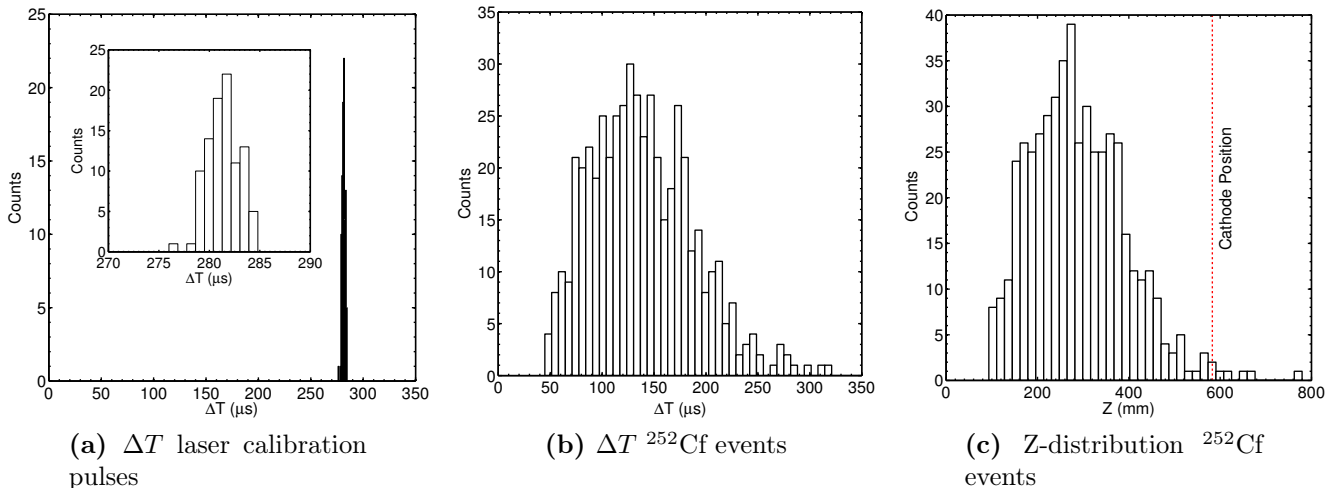


Figure 14: (a) Distribution of the time difference between secondary, SF_5^- , and primary, SF_6^- peaks (ΔT) for the laser calibration pulses obtained in 30 Torr SF_6 and $E = 1029 \text{ V}\cdot\text{cm}^{-1}$. (b) The same distribution for triggered events that passed analysis cuts from the ^{252}Cf data shows a broad distribution of Z locations. (c) The distribution of the Z locations of events from the ^{252}Cf run after analysis cuts. The vertical line shows the position of the cathode at $Z = 58.3 \text{ cm}$. The events with Z locations greater than the cathode location are those that misidentified peaks. There are no events below 10 cm due to the fact that the two peaks are not separable for drift distances less than this.

7 Event fiducialization

7.1 ^{252}Cf data

We showed in Figure 2 of Section 3.2 that at high drift fields, the waveform of the charge arriving at the anode consists mainly of the two SF_5^- and SF_6^- peaks. Having two or more species of charge carriers with differing mobilities is critical for event fiducialization in gas-based TPCs employed in dark matter and other rare event searches. The ability to fiducialize in these experiments allows for the identification and removal of the most pernicious backgrounds, which originate at or near to the inner surfaces of the detector. While identifying the event location in the readout plane (X,Y) of a TPC is straightforward, locating the event along its drift direction (Z) is challenging. Unlike in accelerator-based experiments, the time of interaction (T_0) in a gas-based TPC used for rare searches is not available, so Z-fiducialization had proven difficult. The recent discovery of minority charge carriers in $\text{CS}_2 + \text{O}_2$ mixtures [19], has changed this by allowing the differences in their mobility to be used to derive the Z coordinate of the event. This has transformed the DRIFT dark matter experiment [17], which, until this discovery, had operated for close to a decade with backgrounds from radon progeny recoils at the TPC cathode that severely impacted the dark matter search [16, 76, 77, 78, 79].

The differences in the SF_5^- and SF_6^- mobilities in pure SF_6 can be used in a similar manner to measure the Z coordinate of the event through the relation:

$$Z = \frac{v_s \cdot v_p}{v_s - v_p} \Delta T, \quad (20)$$

where v_p and v_s are the drift speeds of the negative ions in the primary (SF_6^-) and secondary (SF_5^-) peaks, respectively, and ΔT is the time separation of the peaks. Note that the anode (THGEM) is at $Z = 0$, and the cathode at $Z = 58.3 \text{ cm}$.

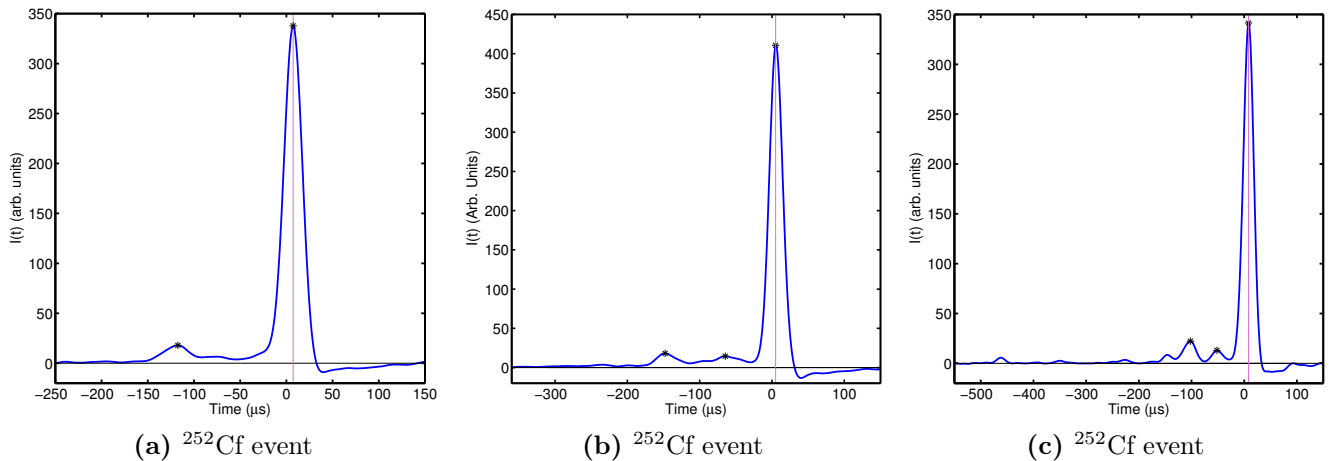


Figure 15: (a) An event from the ^{252}Cf run in 30 Torr SF_6 and $E = 1029 \text{ V}\cdot\text{cm}^{-1}$ showing two distinct peaks. The black markers identify the locations of peaks detected by peak finding algorithm. The magenta vertical line passing through the black marker passes through the location of the primary, SF_6^- , peak. (b) An event from the same data run with three detected peaks. (c) An event with as many as five peaks; three are detected by the peak finding algorithm.

To test how well one can determine the location of events in SF_6 using this method, we used a ^{252}Cf source to generate ionization events at different locations in the detection volume. The ^{252}Cf source was placed near the outside surface of the vessel and about 20 cm from the cathode. The detector was operated at 30 Torr with $E = 1029 \text{ V}\cdot\text{cm}^{-1}$ where the highest gas gains were achieved (Section 6). This was important for identifying the small SF_5^- peak in low energy recoils, which produce less ionization than the nitrogen laser illuminating the cathode. Preceding the ^{252}Cf run, an energy calibration was done with an internally mounted ^{55}Fe source. In addition, to calibrate ΔT we pulsed the laser onto the cathode to generate ionization from a known, fixed Z location.

The SF_5^- and SF_6^- peaks were found through an automated process using a derivative based peak finding algorithm. Although the algorithm performs efficiently for a large data-set, the derivative based approach tends to give false peak detections for noisy data. To reduce the chance of false peak detections affecting the accuracy of Z , we only accepted events that have two and only two identified peaks, one corresponding to SF_5^- and the other to SF_6^- . This greatly reduced the efficiency of our analysis, but our aim here was only to demonstrate event fiducialization in SF_6 , with work on increasing the efficiency left for future work. In addition, only events with energy $> 60 \text{ keVee}$ were accepted so that the SF_5^- peaks were more easily identified, and also to better aid discrimination against electronic recoils due to the gamma-rays from the ^{252}Cf source.

The distribution of the time difference, ΔT , between the SF_5^- and SF_6^- peaks for the laser calibration data is shown in Figure 14a. The distribution has a mean of $281.3 \mu\text{s}$ (583.5 mm) and FWHM of about $3.5 \mu\text{s}$ (7.3 mm), demonstrating the fundamental accuracy and precision of fiducialization in SF_6 . The distribution of the same timing parameter from the ^{252}Cf run is shown in Figure 14b. The mean and shape of the distribution grossly agree with expectations based on the location of the source, which results in a larger solid angle intersecting the detector volume on the anode side. Note that there are no events seen with $Z < 10 \text{ cm}$ because the SF_5^- and SF_6^- peaks cannot be resolved individually at low Z by our simple peak finding algorithm.

A sample event from the ^{252}Cf exposure with a relatively well-defined SF_5^- peak is shown in Figure 15a, demonstrating the feasibility of fiducialization on an event by event basis. Also note that the relative amplitude of the SF_5^- and SF_6^- peak in this event is 5.3%, higher than the

laser generated ionization data from Section `refsec:relativeratios` at the same reduced field, and for some events in our dataset, the relative amplitude exceeded 8%. This could be explained by the fact that the energies of electrons created by a nuclear recoil could be significantly higher than those produced by laser illumination of the cathode, and higher than the energy gained from the drift field before capture.

Examples of events demonstrating this effect is shown in Figures 15b and 15c. These events possess more than two peaks, indicating that other negative ion species besides SF_5^- and SF_6^- are being produced due to the initial energies of liberated electrons. This adds a complication into the analysis to determine the event location, which requires further study. On the other hand, the sensitivity of the relative strength of the SF_5^- , SF_6^- , and other peaks to electron energies could open up possibilities beyond fiducialization. One potential application is for discriminating between electron and nuclear recoils. If the distribution of electron energies created by an electron recoil is characteristically distinct from the one created by a nuclear recoil, than the relative charge in the peaks could be used to identify the type of particle that created the ionization.

7.2 Secondary peak enhancement

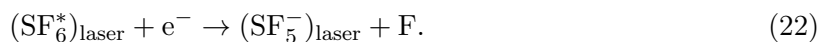
The efficiency with which one can fiducialize in SF_6 is largely dictated by how well the relatively small SF_5^- peak is detected. Here we consider a few possible approaches that might enhance its relative abundance.

The first, motivated by the behavior of the minority peaks in $\text{CS}_2 + \text{O}_2$ gas mixtures [19], is to add a small amount (< 1 Torr to a few Torr) of O_2 into SF_6 . We attempted this and, not surprisingly, saw no significant change in the relative abundance of SF_5^- . Another approach that is motivated by the energy dependence of the SF_5^- and SF_6^- production cross-sections, which favors a larger $\text{SF}_5^-/\text{SF}_6^-$ ratio at higher electron energies, is to operate at higher reduced drift fields. Depending on how high one needs to operate at, this could increase diffusion to unacceptable levels (Figure 9a).

Perhaps, the most straightforward path, however, is to increase the gas gain, thereby increasing the overall signal-to-noise for detecting the SF_5^- peak. As the gains in our measurements with a single THGEM are already at or close to the maximum, two or more THGEMs as well as other MPGD amplification devices should be attempted. As discussed at length in Section 6, amplification devices with the highest possible reduced fields are desired to counteract the physical effects in a negative ion gas that compete with avalanche production. This is especially important for SF_5^- , which, due to its high electron affinity, would benefit from high E/p to efficiently strip the electron and initiate the avalanche.

There also exists an interesting alternative method to increase the production of SF_5^- in SF_6 . A study of the production cross-section for SF_5^- by auto-dissociation has shown that the first peak at ~ 0.0 eV is very sensitive to temperature [80]. Over the temperature range 300 K to 880 K, the relative cross-section for the formation of SF_5^- increases by about two orders of magnitude for electron energies ~ 0.0 eV, while the cross-section hardly varies for energies near the second peak at 0.38 eV.

Since increasing the gas temperature effectively raises the vibrational and rotational excitation energy of the SF_6 molecules, this led Ref. [80] to consider the possibility of the photo-enhancement of SF_5^- production via the processes:



Using a CO_2 laser (9.4 – 10.6 μm) to vibrationally excite SF_6 molecules, they observed an enhancement of SF_5^- production that was radiation wavelength dependent and different for ^{32}S and

^{34}S isotopes. It should be noted that infrared excitation should not result in photodetachment of the SF_6^- anion as measurements have shown that the threshold for this process is at 3.16 eV (392 nm) [81]. Nevertheless, implementing this idea or increasing the gas temperature for large TPCs presents practical challenges that must be weighed against any benefit. These are experimental questions that require further investigation.

8 Conclusion

We have shown that gas gain is achievable in a low pressure gas detector with SF_6 as the bulk gas. Signals from low energy ^{55}Fe events were detected using a 0.4 mm and 1.0 mm THGEM with a gain of between 2000 – 3000. The energy resolution appear to depend on the reduced field in the amplification region, implying that electron detachment and re-attachment in the avalanche region could be responsible. Testing other GEM geometries and amplification devices in SF_6 to achieve even better gain and energy resolution could be the subject for future work. The acrylic cylindrical detector design allowed for high reduced field operation and made possible the detection of interesting behavior and features in SF_6 , particularly the evolution of the waveform shape with reduced field and the identification of the SF_5^- peak through its mobility. Using this secondary peak, we showed that fiducializing events in the drift direction is possible. Diffusion measurements showed thermal behavior for both SF_6 and CS_2 , but only up to a critical reduced field. This has important implications for the optimization of tracking detectors utilizing these negative ion gases. Some features and behavior remained unexplained, but these unanswered questions should provide ample motivation and opportunities for future studies on the use of SF_6 in TPCs.

Acknowledgements

This material is based upon work supported by the NSF under Grant Nos. 1103420 and 1407773.

References

- [1] R. W. Crompton and G. N. Haddad, *Aust. J. Phys.* 36, 15-25 (1983).
- [2] D. Smith, N. G. Adams and E. Alge, *J. Phys. B: At. Mol. Phys.* 17, 461 (1984).
- [3] Z. L. Petrovic and R. W. Crompton, *J. Phys. B* 17, 2777-2791 (1985).
- [4] T. M. Miller, A. E. Stevens Miller, J. F. Paulson, and Xifan Liu, *J. Chem. Phys.* 100, 8841 (1994).
- [5] P. G. Datskos, L. G. Christophorou, and J. G. Carter, *J. Chem. Phys.* 99, 8607 (1993).
- [6] P. Spanel, S. Matejcik and D. Smith, *J. Phys. B: At. Mol. Opt. Phys.* 28, 2941 (1995).
- [7] M. Braun, C. Barsotti, S. Marienfeld, E. Leber, M.-W. Ruf, and H. Hotop, *Eur. Phys. J. D* 35, 177 (2005).
- [8] A. A. Viggiano, T. M. Miller, J. F. Friedman, and J. Troe, *J. Chem. Phys.* 127, 244305 (2007).
- [9] R. L. Merlino and S.-H. Kim, *J. Chem. Phys.* 129, 224310 (2008).
- [10] L. G. Christophorou, J. K. Olthoff, and D. S. Green, *NIST Technical Note* 1425 (1997).
- [11] L. G. Christophorou and J. K. Olthoff, *J. Phys. Chem. Ref. Data*, Vol. 29, No. 3 (2000).
- [12] P. Camarri et al., *Nucl. Instr. and Meth A* 414 (1998) 317.

- [13] G. Aielli et al., Nucl. Instr. and Meth A 493 (2002) 137.
- [14] D. R. Nygren, Journal of Physics: Conference Series 65 (2007) 012003.
- [15] C. J. Martoff et al., Nucl. Instrum. Methods Phys. Res. A 440, 355 (2000).
- [16] S. Burgos et al., Astroparticle Physics, 28 (4-5) (2007), pp. 409–421.
- [17] J. B. R. Battat et al., "First background-free limit from a directional dark matter experiment: results from a fully fiducialised DRIFT detector" , Phys. Dark Univ. 9–10 (2015) 1-7.
- [18] J. Ellis and R. A. Flores, Phys. Lett. B 263, 259 (1991).
- [19] D. P. Snowden-Ifft, Rev. Sci. Instrum. 85, 013303 (2014).
- [20] S. J. Cavanagh, S. T. Gibson, and B. R. Lewis, J. Chem. Phys. 137, 144304 (2012).
- [21] L. G. Christophorou and J. K. Olthoff, Int. J. Mass Spectr. 205 (2001) 27.
- [22] E.P. Grimsrud, S. Chowdhury, P. Kebarle, J. Chem. Phys. 83 (1985) 1059.
- [23] E. C. M. Chen, J.R. Wiley, C.F. Batten, W.E. Wentworth, J. Phys. Chem. 98 (1994) 88.
- [24] NIST Standard Reference Database 69: NIST Chemistry WebBook.
- [25] L. G. Christophorou, "Insulating Gases," Nuclear Instruments and Methods in Physics Research, Vol. A268, pp. 424-433, 1988.
- [26] L. G. Christophorou and S. R. Hunter, "From Basic Research to Applications", in Electron-Molecule Interactions and Their Applications, L. G. Christophorou (Ed.), Academic Press, NY, Vol. 2, Chap. 5, 1982.
- [27] Th. Aschwanden, "Swarm Parameters in SF6 and SFe/N2 Mixtures Determined from a Time Resolved Discharge Study", in Gaseous Dielectrics IV, L. G. Christophorou and M. O. Pace (Eds.), Pergamon Press, NY, pp. 24-32, 1984.
- [28] W. P. Wood, J. Heicklen, J. Phys. Chem., 1971, 75 (7), pp 861-866.
- [29] D. R. Nygren, 7th Symposium on large TPCs for low-energy rare event detection, Paris (2014).
- [30] D. Edelson, J. E. Griffiths, and K. B. McAfee, Jr., J. Chem. Phys. 37, 917 (1962).
- [31] R. N. Compton, L. G. Christophorou, G. S. Hurst, and P. W. Reinhardt, J. Chem. Phys. 45, 4634 (1966).
- [32] P. W. Harland and J. C. J. Thynne, J. Phys. Chem. 75, 3517 (1971).
- [33] L. G. Christophorou, *Atomic and Molecular Radiation Physics* (Wiley, New York, 1971), Ch. 6.
- [34] L. G. Christophorou, Adv. Electron, Electron Phys. 46, 55 (1978).
- [35] L. G. Christophorou, D. L. McCorkle, and A. A. Christodoulides, Electron-Molecule Interactions and Their Applications, edited by L. G. Christophorou (Academic, New York, 1984), Vol. 1, Chap. 6.
- [36] J. M. S. Henis and C. A. Mabie, J. Chem. Phys. 53, 2999 (1970).
- [37] R. W. Odom, D. L. Smith, and J. H. Futrell, J. Phys. B 8, 1349 (1975).
- [38] M. S. Foster and J. L. Beauchamp, Chem. Phys. Lett. 31, 482 (1975).
- [39] E. W. McDaniel, E. A. Mason, The Mobility and Diffusion of Ions in Gases, John Wiley & Sons, USA, 1973.
- [40] B. Lehmann, Z. Naturforsch. 25A (1970) 1755.

- [41] M. V. V. S. Rao, S. K. Srivastava, in: T. Andersen, B. Fastrup, F. Folkmann, H. Knudsen (Eds.), Proceedings of the 18th International Conference on the Physics of Electronic and Atomic Collisions, Aarhus, Denmark, July 21-27, 1993, Abstracts of contributed papers, p. 345.
- [42] L. E. Kline, D. K. Davies, C. L. Chen, P. J. Chantry, J. Appl. Phys. 50 (1979) 6789.
- [43] L. G. Christophorou and J. K. Olthoff, Int. J. Mass Spectrom., 205 (2001) 27-41.
- [44] H. Hotop, D. Klar, J. Kreil, M.-W. Ruf, A. Schramm, J. M. Weber, in: L. J. Dube, J. B. A. Mitchell, J. W. McConkey, C. E. Brion (Eds.), The Physics of Electronic and Atomic Collisions, AIP Conference Proceedings, vol. 360, AIP Press, Woodbury, New York, 1995, p. 267.
- [45] D. Klar, M.-W. Ruf, H. Hotop, Aust. J. Phys. 45 (1992) 263.
- [46] X. Ling, B. G. Lindsay, K. A. Smith, F. B. Dunning, Phys. Rev. A 45 (1992) 242.
- [47] S. R. Hunter, J. G. Carter, L. G. Christophorou, J. Chem. Phys. 90 (1989) 4879.
- [48] P. L. Patterson, J. Chem. Phys. 53, 696 (1970).
- [49] J. de Urquijo-Carmona, I. Alvarez, H. Martinez, and C. Cisneros, J. Phys. D 24, 664 (1991).
- [50] I. A. Fleming and J. A. Rees, J. Phys. B: At. Mol. Phys. 2 777-9 (1969).
- [51] Y. Wang, R. L. Champion, L. D. Doverspike, J. K. Olthoff, and R. J. van Brunt, J. Chem. Phys. 91, 2254, (1989).
- [52] A. A. Christodoulides, D. L. McCorkle, and L. G. Christophorou, in *Electron-Molecule Interactions and Their Applications*, edited by L. G. Christophorou (Academic, New York, 1984), Vol. 2, Chap. 6.
- [53] J. K. Olthoff, R. J. van Brunt, Y. Wang, R. L. Champion, and L. D. Doverspike, J. Chem. Phys. 91, 2261 (1989).
- [54] R. L. Champion, in *Gaseous Dielectrics VI*, edited by L. G. Christophorou and I. Sauers, (Plenum, New York, 1991), p. 1.
- [55] H. Haberland, H. Langosch, H.-G. Schindler, and D. R. Worsnop, J. Phys. Chem. 88, 3903-3904 (1984).
- [56] H. Haberland, C. Ludewigt, H.-G. Schindler, and D. R. Worsnop, J. Chem. Phys. 81 (8) (1984).
- [57] W. B. Knighton, D.R. Zook, E. P. Grimsrud, J. Am. Soc. Mass Spectrom. 1 (1990) 372-81.
- [58] L. W. Sieck, J. Phys. Chem. 90 (1986) 6684-6687.
- [59] S. T. Arnold and A. A. Viggiano, J. Phys. Chem. A 105 (2001) 3527-3531.
- [60] D. P. Snowden-Ifft and J.-L. Gauvreau Rev. Sci. Instrum. 84, 053304 (2013).
- [61] W. Blum and L. Rolandi, "Particle Detection with Drift Chambers", New York: Springer-Verlag (1994).
- [62] E. A. Mason and E. W. McDaniel, *Transport Properties of Ions in Gases* (Wiley, New York, 1988).
- [63] L. A. Viehland and E. A. Mason, Atomic Data and Nuclear Data Tables 60, 37-95 (1995).
- [64] F. Mayet et al., Physics Reports 627 (2016) 1-49.
- [65] E. Krishnakumar and K. Nagesha, J. Phys. B: At. Mol. Opt. Phys. 25, 1645 (1992).
- [66] S. A. Rangwala, S. V. K. Kumar, and E. Krishnakumar, Phys. Rev. A 64, 012707 (2001).

- [67] D. P. Snowden-Ifft et al., Neutron recoils in the DRIFT detector, Nucl. Instr. Meth. A 498 (1-3) (2003) 155-164.
- [68] J. Miyamoto et al., GEM operation in negative ion drift gas mixtures, Nucl. Instr. Meth. A 526 (2004) 409-412.
- [69] I. Giomataris, R. De Oliveira, S. Andriamonje, S. Aune, G. Charpak, P. Colas, G. Fanourakis, E. Ferrer, A. Giganon, Ph. Rebourgeard, P. Salin, Micromegas in a bulk, Nucl. Instr. Meth. A 560 (2006) 405-408.
- [70] M. P. Dion, C. J. Martoff, and M. Hosack, Astroparticle Physics 33 (2010) 216-220.
- [71] Y. H. Hilal and L. G. Christophorou, J. Phys. D: Appl. Phys. 20 (1987).
- [72] I. Lopes, H. Hilmert, and W. F. Schmidt, J. Phys. D: Appl. Phys. 19 (1986).
- [73] L. G. Christophorou, "Atomic and Molecular Radiation Physics", New York: Wiley-Interscience (1971).
- [74] C. Blondel, P. Cacciani, C. Delsart, R. Trainham, Phys. Rev. A 40, 3698 (1989).
- [75] A E. Stevens Miller, T. M. Miller, A. A. Viggiano, R. A. Morris, J. M. Van Doren, S. T. Arnold, and J. F. Paulson, J. Chem. Phys., 102(22), 8865 (1995).
- [76] J. Brack et al., JINST 9 P07021 (2014).
- [77] J. B. R. Battat et al., JINST 9 P11004 (2014).
- [78] J. B. R. Battat et al., Nucl. Instr. Meth. Phys. Res. A 794 (2015) 3346.
- [79] J. Brack et al., Phys. Procedia 61 (2015) 130-137.
- [80] C. L. Chen and P. J. Chantry, J. Chem. Phys. 71 (1979) 3897.
- [81] P. G. Datskos, J. G. Carter, and L. G. Christophorou, Chem. Phys. Lett. 239, 38 (1995).